UC San Diego

UC San Diego Electronic Theses and Dissertations

Title

The population perspective : how primate retinal ganglion cells collectively encode visual space

Permalink

https://escholarship.org/uc/item/05m1k9j3

Author

Gauthier, Jeffrey Lee

Publication Date

2008

Peer reviewed|Thesis/dissertation

eScholarship.org Powered by the California Digital Library
University of California

UNIVERSITY OF CALIFORNIA, SAN DIEGO

The Population Perspective–How Primate Retinal Ganglion Cells Collectively Encode Visual Space

A dissertation submitted in partial satisfaction of the
requirements for the degree
Doctor of Philosophy

in

Neurosciences

by

Jeffrey Lee Gauthier

Committee in charge:

Professor Edward M. Callaway, Chair
Professor Eduardo J. Chichilnisky
Professor Marla B. Feller
Professor Harvey J. Karten
Professor David H. Rapaport

2008

Copyright
Jeffrey Lee Gauthier, 2008
All rights reserved.

The Dissertation of Jeffrey Lee Gauthier is approved, and it is acceptable in quality and form for publication on microfilm:

_____

_____

_____

_____

_____

Chair

University of California, San Diego

2008

DEDICATION

To Edwin Daniel Karn.

EPIGRAPH

"Begin at the beginning," the King said, very gravely.
"And go on till you come to the end: then stop."
—Lewis Carroll

I only have eyes for you.
—Al Dubin

TABLE OF CONTENTS

Signature Page iii

Dedication iv

Epigraph v

Table of Contents vi

Acknowledgements viii

Vita and Publications x

Abstract xi

Chapter 1 Introduction 1

Chapter 2 Receptive Field Overlap 4
2.1 Introduction 4
2.2 Results 6
2.2.1 Receptive field mosaics of parasol and midget cells 6
2.2.2 Overlap of neighboring receptive field centers . . . 6
2.2.3 Overlap of neighboring receptive field profiles . . . 7
2.3 Discussion 8
2.3.1 Functional vs. anatomical overlap 8
2.3.2 Signal redundancy in parallel visual pathways . . 9
2.4 Methods 11
2.4.1 Preparation and Spike Recording 11
2.4.2 RF Characterization 11
2.4.3 Cell Type Classification and Identification 12
2.4.4 Coverage 13
2.4.5 RF Profiles 13
2.5 Acknowledgements 15

Chapter 3 Receptive Field Interlocking 19
3.1 Introduction 20
3.2 Results 20
3.3 Discussion 24
3.4 Methods 25
3.4.1 Summary. 25
3.4.2 Tissue Preparation. 26
3.4.3 RF Characterization. 26
3.4.4 The Uniformity Index. 26

3.4.5 Rotation Plot (Fig. 3.4a-d). 27
3.4.6 Generation of Simulated RFs. 28
3.5 Acknowledgements 29

Chapter 4 Single Cone Inputs 34
4.1 Introduction 34
4.2 Results 36
4.2.1 Fine RFs reveal single cone inputs 36
4.2.2 Neighboring midget cells share cone inputs 37
4.3 Discussion 38
4.3.1 Extent of midget cone sampling 38
4.3.2 Number of cones sampled by each midget cell . . 39
4.3.3 Sharing of cones by individual midget ganglion cells 40
4.4 Methods 41
4.4.1 Physiological recording and RF characterization . 41
4.4.2 Cone labeling 41
4.4.3 Cone labeling and alignment 42
4.4.4 S cone identification 42

Chapter 5 Summary 47

Works Cited 48

ACKNOWLEDGEMENTS

I would like to thank all those who have impacted my life and career on the way to this dissertation, though words cannot do justice to what they mean to me.

Friends and colleagues in the Neurosciences and Computational Neurobiology graduate programs have been an endless source of encouragement, diversion, and (often) friendly competition.

An important counterpoint to all things Neuroscience was found in Sacred Harp singings and singers from across the country, as well as the beautiful rhythms, dances, and songs of Ghana that were enjoyed with Ho Asogli.

Early mentorship for an indecisive and self-doubting young first year was generously provided by Bill Kristan.

Baptism by fire in the fierce realm of all-night experiments was gleefully administered by former members of the Chichilnisky lab, including Rachel Kalmar, Valerie Uzzell, Eric Frechette, Jessica, and Brook.

I have always received excellent guidance, helpful suggestions, and shrewd advice from my current and past committee members, Ed Callaway, Marla Feller, Harvey Karten, David Rapaport, and Chuck Stevens.

At all stages, my lab mates have made research more interesting, productive, and fun. Thanks to Anastasia Anishchenko, Justin Elstrott, Greg Field, Martin Greschner, Lauren Hruby, Tim Machado, Sasha Sher, Jon Shlens, and Clare Hulse.

For an advisor, I could not have wished for a better mentor and friend than E.J. Chichilnisky.

It goes without saying that I couldn't have done any of this without Claire.

Finally, I thank my family for their support, understanding, free room and board, email updates, phone calls, newspaper clippings documenting virtually all affairs—public and private—of northeastern Wisconsin, and love.

Access to retinas was generously provided by Ed Callaway, Howard Fox, Michael Taffe, and Kent Osborn.

Chapter 2, in full, has been submitted for publication of the material as it may appear in Neuron, 2008, Gauthier, Jeffrey L; Field, Greg D; Sher, Alexander; Greschner, Martin; Shlens, Jonathon; Litke, Alan M; and Chichilnisky, Eduardo

J, Cell Press, 2008. The dissertation author and Greg D Field were the primary investigators and authors of this paper.

Chapter 3, in full, has been submitted for publication of the material as it may appear in PLoS-Biology, 2008, Gauthier, Jeffrey L; Field, Greg D; Sher, Alexander; Greschner, Martin; Shlens, Jonathon; Litke, Alan M; and Chichilnisky, Eduardo J. The dissertation author was the primary investigator and author of this paper.

VITA

2002	B. S. in Mathematics, University of Chicago
2004-2005	Graduate Teaching Assistant, University of California, San Diego
2008	Ph. D. in Neurosciences, University of California, San Diego

PUBLICATIONS

Shlens, J, Field, GD, **Gauthier, JL**, Grivich, MI, Petrusca, D, Sher, A, Litke, AM, and Chichilnisky, EJ. "The Structure of Multi-Neuron Firing Patterns in Primate Retina." *J Neurosci* 26, no. 32 (2006): 8254-66.

Petrusca, D, Grivich, MI, Sher, A, Field, GD, **Gauthier, JL**, Greschner, M, Shlens, J, Chichilnisky, EJ, and Litke, AM. "Identification and Characterization of a Y-Like Primate Retinal Ganglion Cell Type." *J Neurosci* 27 no. 41 (2007): 11019-27.

∗Field, GD, ∗Sher, A, ∗**Gauthier, JL**, Greschner, M, Shlens, J, Litke, AM, and Chichilnisky, EJ. "Spatial Properties and Functional Organization of Small Bistratified Ganglion Cells in Primate Retina", *J Neurosci*, 27, no. 48 (2007): 13261-72.

∗ indicates equally contributing authors

ABSTRACT OF THE DISSERTATION

The Population Perspective–How Primate Retinal Ganglion Cells Collectively Encode Visual Space

by

Jeffrey Lee Gauthier
Doctor of Philosophy in Neurosciences

University of California San Diego, 2008

Professor Edward M. Callaway, Chair

Vision begins in the retina, where populations retinal ganglion cells (RGCs) collectively encode all visual information reaching the brain. RGC encoding is based on the spatial, temporal, and chromatic properties of the receptive field (RF) of each cell. Within each RGC type, RFs are arranged in a regularly spaced lattice that spans the visual field. While much is known about the functional properties and circuitry of individual RFs, the organization of the population has remained elusive. This dissertation employs a recently introduced methodology to make simultaneous, large scale recordings from isolated patches of primate retina. These recordings allow many features of the population level organization of RGCs to be appreciated for the first time.

The output of the primate retina is numerically dominated by four RGC types: ON- and OFF-parasol cells and ON- and OFF-midget cells, which respectively form the major inputs to the magnocellular and parvocellular pathways. The spatial arrangement of these cell types is studied in several important regards. First, Chapter 2 demonstrates that the average RF overlap is nearly identical in all four

types. This echoes the result of a previous study that found nearly the same degree of overlap in several RGC types in the rabbit retina. However, such homogeneity is surprising given the very different anatomical organization of parasol and midget cells and their diverse roles in visual encoding.

Chapter 3 explores the fine shape of individual RFs. Previous studies have found irregularly shaped RFs, and concluded that this "noise" in retinal organization was likely detrimental to visual coverage. However, appreciating the arrangement of a full population revealed that individual RF shapes interlock like puzzle pieces to provide more uniform coverage of visual space. This finding bears an interesting relationship to RGC anatomical organization, and might point to novel developmental mechanisms.

Finally, the organization of midget cells is studied at its elementary resolution: individual cone inputs to the RF. Chapter 4 reveals that midget RFs can sample the same cones as neighboring cells, a finding with several implications for the anatomical and functional organization of the midget cell pathway.

Chapter 1

Introduction

At the end of the 19th century, a foundational debate was shaping the field that would evolve into modern day Neuroscience. What was the fundamental material of the brain? Was the whole brain a single, continuous body, that is, a "syncytium" or "reticulum"? Or was the brain instead a collection of individual cells, each operating independently of its neighbors but always in close communication? Ultimately, the question was decided by images of microscopic brain structures. A new staining technique revealed that the nervous system was composed of individual units, now known as "neurons", whose filamentous, intricate processes could be observed for the first time. The conclusion was accepted almost unanimously, and a Nobel Prize was not long in coming.

But this discovery raised a yet greater problem: How do the many individuals create the whole? That is, how do properties of single neurons combine and interact to generate emergent properties of the network and the brain? Then, as now, the primary limitation to understanding population organization was technical. Just as Golgi staining could highlight a single cell in the dense, tangled mesh of brain matter, so was it utterly unable to reveal how the shapes of neighboring cells wove together. It is a truism, though perhaps a founded one, that the scientific imagination is unavoidably limited by the bounds of available data. The foundational discovery of individual cells, and the subsequent focus on the individual rather than the whole, left a legacy that has ever since shaped the questions and answers to be found Neuroscience.

Still today, population organization remains among the greatest gaps in the knowledge of the nervous system. Many theories explain the role of single neurons as the fundamental agents of computation (e.g. the "grandmother cell" hypothesis [1], place cells [2], single neuron models of limb movement [3], perception correlated with single cell firing rate [4]), but far fewer elaborate on how individual properties interact to benefit the larger network or organism (e.g. a link between Hebbian learning and visual map formation [5]).

In many respects, an excellent model system for understanding populations of neurons, and in particular how individual cells relate to the larger whole, is found in the retina. Retinal ganglion cells (RGCs) are the only output from the retina to the brain, and later stages of visual neurons pool RGC responses at all spatial and temporal scales, meaning that RGC populations are sure to exhibit carefully evolved and exquisitely tuned population interactions. In addition, RGCs can be classified into several well defined types, each type operating in parallel and sending its unique message to a distinct part of the brain. Within each type, RGCs form a regularly spaced lattice, giving each cell a precisely defined neighborhood in which to study neighbor interaction. Finally, RGCs are located on the edge of the retina, typically arranged in a single layer, making them among the most accessible neurons in the central nervous system.

Early studies revealed that each RGC is sensitive to light in a small region of visual space known as the "receptive field" (RF, [6, 7]). Probing the shape of RFs with small spots revealed a roughly circular structure, with an excitatory central region and inhibitory surround, and this model has persisted up to the present day [8]. Concurrently, anatomical studies revealed that the cells of each RGC class are arranged in a regularly spaced lattice, or mosaic [9]. Thus an understanding of RGCs at the population level is really an understanding of mosaic organization.

This dissertation presents several recent discoveries about the organization of RF mosaics. Chapter 2 characterizes how much RFs overlap with neighbors, a feature that is central to understanding how information in a visual image is divided among the many cells that encode it. This chapter follows closely on previous work characterizing RF overlap in other species [10–13], but expands in an important

direction: focusing on cell types which participate in known visual pathways and for which anatomical organization is well characterized.

Chapter 3 breaks new ground in understanding the fine structure of RF mosaics. Previous measurements [14–16] have shown that RFs have irregular shapes which resemble a "noisy" attempt at a smooth Gaussian dome. However, when observing a full population of RFs, the irregular shapes are seen to fit together like puzzle pieces. This surprising coordination shows that neural populations can be organized at a much finer scale than previously appreciated.

Finally, Chapter 4 refines the descriptions of Chapters 2 and 3 the finest possible level of detail: the single cone inputs to each RGC. This chapter explores the single cone sampling by a local mosaic of midget cells, the highest spatial resolution pathway in primates [17]. Its findings suggest that midget cell RFs might be precisely arranged at the level of single cone inputs.

Appreciating the trends in past century of Neuroscience, an interesting reversal seems ready to take place. Though the founding debate decided sharply in favor of the importance of individual neurons, today a new movement can be seen emerging, to which this work hopes to contribute. It is arising from the discovery, in many modalities, in many species, that network interaction and population dynamics are themselves the fundamental units of neural computation. The syncytium is making a comeback.

Chapter 2

Receptive Field Overlap

The collective representation of visual space in the high resolution visual pathways was explored by simultaneously measuring the receptive fields of hundreds of ON and OFF midget and parasol ganglion cells in isolated primate retina. As expected, the receptive fields of all four cell types formed regular mosaics uniformly tiling the visual scene. Surprisingly, comparison of all four mosaics revealed that the overlap of neighboring receptive fields was nearly identical, for both the excitatory center and inhibitory surround components of the receptive field. These observations contrast sharply with the large differences in the dendritic overlap within the parasol and midget cell populations, revealing a surprising relationship between the anatomical and functional architecture in the dominant circuits of the primate retina.

2.1 Introduction

Populations of sensory neurons encode information collectively, and a fundamental aspect of the population code is *signal redundancy*, i.e. the degree to which features of sensory space are represented by more than one neuron. In the mammalian retina, roughly 20 types of retinal ganglion cells (RGCs) sample visual space [18, 19], and each cell type forms a lattice of regularly spaced receptive fields (RFs) that could overlap to a greater or lesser degree [10–13]. Greater RF overlap implies greater signal redundancy in the neural encoding [13, 20], which may be

valuable for downstream computations that are sensitive to noise, but may also be less efficient. In the primate visual system, distinct lines of evidence make conflicting predictions about the degree of signal redundancy in the magnocellular and parvocellular pathways, which provide the highest resolution visual signals to the brain and are a major focus of current research.

Anatomical studies predict a substantial difference in the signal redundancy of parasol and midget retinal ganglion cells [21,22] which form the dominant input to the magnocellular and parvocellular pathways, respectively [23–26]. The dendritic fields (DFs) of parasol cells overlap extensively, while midget cell DFs exhibit no overlap [26–28], as depicted in Figure 3.2A. If the RFs of these populations exhibited a correspondingly large difference in overlap, parasol cells would sample the visual scene with high signal redundancy, while midget cells would provide more independent samples, perhaps reflecting their distinct roles in vision [29].

A very different prediction, however, arises from physiological measurements in rabbit retina. One study [11] revealed nearly identical RF overlap among several diverse types of ganglion cells (but see [12]). This finding suggests that a single degree of signal redundancy can satisfy a variety of visual processing requirements. A possible prediction is that parasol and midget cells also exhibit a common degree of signal redundancy that is optimal for both magnocellular and parvocellular pathways, despite their apparently divergent visual functions. Although the receptive field structure of individual parasol and midget cells has been examined previously ([30], see [31]), the signal redundancy in these cell populations has not.

We examined the collective representation of visual space in populations of parasol and midget ganglion cells by applying large-scale electrophysiological recordings to isolated peripheral primate retina [32,33]. Within the regular mosaic formed by each cell type, ON and OFF midget and parasol cells exhibited nearly identical RF overlap, in both the center and surround components of the RF, in striking contrast to substantial differences in their DF overlap. These findings reveal a surprising relationship between anatomical structure and functional organization, and suggest that common rules may govern collective encoding in the parvocellular and magnocellular pathways.

2.2 Results

2.2.1 Receptive field mosaics of parasol and midget cells

Light responses of hundreds of retinal ganglion cells were simultaneously recorded in isolated segments of macaque monkey retina. The receptive field (RF) of each cell was identified using reverse correlation with a white noise stimulus [34]. Cells were functionally classified as ON and OFF parasol and midget based on their light response properties and density [35]. To visualize RFs, the center component was extracted from a difference of Gaussians fit to the spatial sensitivity profile (see Methods; [36]). The RF center boundary was represented graphically by the 1 SD contour of the Gaussian fit [11]. This definition of the RF spatial extent, though arbitrary, permits a standardized comparison between RFs of different cell types. Figure 3.2B,C shows the RF centers of simultaneously recorded ON and OFF parasol and midget cells from two preparations. As expected from previous work [26, 28, 34, 33, 35], the RFs of each cell type formed a regularly spaced lattice, or mosaic. The observed mosaic structure indicates that, over some regions of retina, all or nearly all cells of each type were recorded. This complete sampling is essential for reliably measuring the signal redundancy in each cell type.

2.2.2 Overlap of neighboring receptive field centers

Visual inspection of Figure 3.2B,C suggests that parasol and midget RFs exhibit similar RF overlap. Specifically, the RFs of all four cell types appear to abut their neighbors at approximately the 1 SD boundary shown by the outlines. Note that this does not imply no overlap of RFs: a substantial fraction of the RF lies outside the 1 SD boundary. However, the similar pattern across cell types suggests equal overlap.

The suggestion of equal overlap was confirmed quantitatively by measuring the spacing of cells in each mosaic, relative to the size of the RFs. Specifically, the distance between neighboring RF centers was divided by the equivalent RF radius, producing a normalized nearest neighbor distance (NNND; see Methods, [11]). For a mosaic with high (low) overlap, the NNND will be small (large). When

neighboring RFs just touch at the 1 SD boundary, the NNND value is 2. Figure 2.2A shows the NNNDs for each cell type from the preparation of Figure 3.2B. The modal NNND of each cell type is represented graphically beneath the abscissa. For all four cell types, the modal NNND was near 2, confirming the impression that the RFs of neighboring cells abut roughly at the 1 SD outline. Figure 2.2B shows similar results for the preparation of Figure 3.2C.

Parasol and midget cells exhibited nearly identical RF overlap in multiple recordings over a range of eccentricities. Figure 2.2C shows modal NNNDs of parasol and midget cells, summarizing the RF overlap of 36 mosaics (3,221 cells spanning 10 retinas). ON and OFF populations are represented by open and closed circles, respectively. The data fall near the identity line (solid line) that indicates equal RF overlap. This finding contrasts with the approximately two-fold difference predicted from DF overlap (dashed line). On average, ON cells exhibited slightly more overlap than OFF cells, for both parasol and midget populations [34]. Figure 2.2D reveals that overlap did not vary with retinal eccentricity across the peripheral visual field. Over the range of eccentricities recorded, RF sizes varied by roughly two-fold. Thus, the observed overlap is a consistent feature that is independent of absolute RF size.

2.2.3 Overlap of neighboring receptive field profiles

The above results were confirmed over the entire extent of the RF, including the inhibitory surround, by directly examining light sensitivity profiles. For each reference cell, light sensitivity was measured along the line connecting the RF center to that of the nearest neighbor in the mosaic, producing two spatial profiles: one for the reference cell, and one for the neighbor. The reference and neighbor profiles were averaged across every reference cell in the mosaic. These profiles were normalized to focus on profile shape independently of absolute size, spacing, and sensitivity (see Methods).

Figure 2.3A shows the resulting average neighbor profiles for ON and OFF parasol and midget cells from the preparation of Figure 3.2C. All four cell types exhibited nearly identical overlap in neighbor profiles, though the ON parasol cells

exhibited a slightly flatter peak, and, as in Figure 2.2C, ON cells exhibited slightly greater overlap. The closely overlaying profiles confirm that RF overlap is nearly equal in all four cell types. Unlike the parametric analysis above, this analysis also shows the contribution of the inhibitory RF surrounds, which overlay closely. Similar results were observed in a second preparation (Figure 2.3B).

2.3 Discussion

ON and OFF parasol and midget cells exhibited nearly identical RF overlap, and thus signal redundancy. This finding resolves conflicting predictions that emerge from previous anatomical and physiological studies. It also has implications for the nature of visual encoding in the high-resolution pathways of the primate visual system, and for the functional architecture of retinal circuits.

2.3.1 Functional vs. anatomical overlap

The nearly identical functional overlap in midget and parasol cells contrasts with striking differences in anatomical overlap (Figure 3.2A): parasol cell DFs overlap substantially, while midget cell DFs overlap little or not at all [26–28]. The disparity between anatomical and physiological overlap indicates that the relationship between RF and DF is not universal, but is unique to each cell type. This specificity presumably reflects the known diversity of the bipolar and amacrine cell circuits contacting each RGC type (see [37]). This issue has arisen in previous studies of the relation between RF and DF structure [38,39,14,15], and the present results unequivocally demonstrate that the form of the RF is strongly influenced by aspects of the retinal circuitry specific to each cell type.

Several factors could contribute to the similarity of RF overlap in midget and parasol cells. First, distal parasol dendrites, being a greater absolute distance from the soma than midget distal dendrites [22,27], might also be a greater electrotonic distance from the spike initiation zone. If they are, then distal parasol dendrites would have less influence on the RF than distal midget dendrites, yielding a relatively narrower parasol cell RF. However, this possibility seems to be contradicted

by a compartmental model of cat ON alpha cells, which suggested that all synapses should be approximately equally effective [40]. Of course, the density of synapses also plays an important role in determining the shape of the RF [41], but synaptic density has not been systematically mapped on midget and parasol cell dendrites. Another possible mechanism is the relative size of bipolar cell RFs. A ganglion cell RF is roughly equivalent to a convolution of its DF with the bipolar cell RFs which feed it [40]. Previous measurements [42] reveal that the RFs of bipolars that provide input to midget cells (midget bipolars, [43]) are a larger fraction of the RGC DF than the RFs of bipolars that provide input to parasol cells (diffuse bipolars, [44]). This difference could explain the comparative narrowness of the parasol cell RF relative to its DF.

2.3.2 Signal redundancy in parallel visual pathways

Previous work presents a complex picture of RF overlap in different RGC types. The first direct measurement of RF overlap revealed striking homogeneity among several RGC types in the rabbit retina [11], and provided a theoretical suggestion that this degree of overlap could be optimal for many RGC types. However, several subsequent studies questioned this conclusion by demonstrating that RF overlap varies significantly across different cell types. One study [12] showed that the densest cell type of the rabbit retina exhibits much higher RF overlap than originally reported [11]. Another recent study in primate retina showed that ON parasol cells have slightly higher RF overlap than small bistratified cells [35], which exhibit a distinctive bistratified dendritic morphology and color-opponent light responses. In the larval tiger salamander, RF overlap seems to vary for different RGC types [13], though cell type classification in this species is less certain. Theoretical work has also suggested that the optimal degree of RF overlap can depend on factors unique to each cell type [45, 46]. Finally, no previous studies have examined the overlap of the full spatial profile, including both the excitatory center and inhibitory surround.

While the present results do not provide a unified view of how or why RF overlap varies across cell types, they unambiguously demonstrate nearly identical RF

overlap in midget and parasol cells, in spite of clearly different anatomical overlap. Furthermore, the complete analysis of RF profiles, including center and surround, indicates that the signal redundancy is nearly identical. The importance of midget and parasol cells for primate vision, and the extensive literature on their function (see [31]) and anatomy (e.g. [22]), enables the measurement of signal redundancy to be interpreted more completely than was possible in previous studies.

Specifically, the similarity of signal redundancy is especially surprising in light of the distinct functional roles of the two pathways. Neurons in the magnocellular and parvocellular layers of the lateral geniculate nucleus (LGN), which receive predominantly parasol and midget inputs, respectively [23–26], exhibit very different projections to visual cortex and systematically different response properties (see [47, 48]). The visual signals carried by these two pathways are thought to mediate largely distinct visual functions, such as perception of change and motion, or fine grained spatial detail and color, respectively [29]. The unique functions of these pathways begin to emerge in the distinct light response properties of individual midget and parasol cells [30, 49–54]. In principle, the different functions of the magnocellular and parvocellular pathways could demand different degrees of signal redundancy in the underlying RGC signals. Instead, the striking similarity suggests that the two high-density pathways may share a common functional requirement – such as the need to efficiently encode visual information in a limited number of optic nerve fibers – and that the observed redundancy may optimally satisfy this requirement.

A perplexing problem raised by the present observations is how developmental mechanisms produce such homogeneous functional organization for the otherwise very different parasol and midget cells. Certainly, anatomical evidence indicates that the mechanisms responsible for dendrite growth must operate differently in the midget and parasol populations. The fact that these mechanisms precisely counterbalance other elements of retinal circuitry, producing nearly identical RF overlap and profiles, suggests that development of RGC dendrites may be governed by the functional outcome, and thus may rely partly on mechanisms that are driven by visual signals [55–57].

2.4 Methods

2.4.1 Preparation and Spike Recording

Retinas were obtained and recorded as described previously [34, 35]. Briefly, eyes were enucleated from terminally anesthetized macaque monkeys (*Macaca mulatta*) from a variety of sources (see [35]) in accordance with institutional guidelines for the care and use of animals. Immediately after enucleation, the anterior portion of the eye and vitreous were removed in room light. Following a dark incubation period, patches of peripheral retina were isolated from the pigment epithelium and placed flat, RGC layer down, on a planar array of 512 extracellular microelectrodes covering an area 1890 μm x 900 μm. During recording, the retina was kept at 33-35°C and was perfused with Ames' solution bubbled with 95% O_2 and 5% CO_2, pH 7.4.

Raw voltage recordings were analyzed offline to isolate the spikes of single cells, as described previously [35]. Briefly, candidate spike events were detected using a threshold on each electrode, and the voltage waveform on the center and nearby electrodes in the vicinity of spike events was saved. Spikes were clustered based on waveform shape, and spike clusters were identified as candidate neurons if they exhibited a refractory period and an average spike rate >1 Hz. Duplicate recordings of the same cell were identified by temporal cross-correlation and removed.

2.4.2 RF Characterization

RFs were mapped as described previously [34,35]. Briefly, the optically reduced image of a gamma-corrected cathode ray tube computer display (Sony Multiscan E100) refreshing at 120 Hz was focused on the photoreceptor outer segments, and low photopic intensity was achieved by neutral density filters in the light path. A white noise stimulus was presented, consisting of a lattice of squares, each flickering randomly and independently at 30 or 120 Hz [58], with the intensities of the red, green, and blue display phosphors within each square varying independently. The contrast of this stimulus for each of the three display phosphors was 96% (SD of modulation divided by mean intensity), and the sidelengths of individual squares

(henceforth, pixels) varied from 30 μm to 60 μm. The RF of each recorded cell was mapped by computing the spike triggered average (STA) stimulus during the white noise presentation (see [59, 58]).

RFs were summarized by fitting with a parametric model. The model consisted of the product of three profiles: spatial, temporal, and chromatic [34]. The temporal profile was a difference of lowpass filters. The spatial profile consisted of a difference of 2-dimensional elliptical Gaussian functions. The chromatic profile was the relative weighting of the three monitor phosphors. Surrounds were relatively weak, so the cell surrounds could not be fitted individually in a robust fashion. However, on average, the STA spatial profile was well described by a fit in which the radius of the surround was twice that of the center. Thus, the following procedure was used to fit the spatial profile. A single two-dimensional Gaussian was fitted to the STA of each cell, generating a rough estimate of receptive field center location and radius. An inhibitory surround was then introduced, and the fit was re-optimized over all remaining parameters, with the surround radius constrained to be twice the center radius. Several parameters of the fit were extracted to visualize RF extent: the location of the Gaussian fit center, the SDs along the major and minor axes, and the angle of the major axis. These parameters defined an ellipse for each cell that represented the 1 SD contour of the Gaussian fit. In figures, receptive field outlines are represented using this contour.

2.4.3 Cell Type Classification and Identification

The anatomical cell type of recorded cells was determined using a two step procedure, as described previously [34, 35]. Briefly, cells were first grouped into functional cell classes based on their light response properties. Correspondences between functional classes and anatomical types were determined by density and light response properties. This procedure definitively identified the ON and OFF parasol and midget cells in each recording.

2.4.4 Coverage

Anatomical coverage of dendritic fields is usually defined as the average number of cells sampling any given point in visual space. In the case of receptive fields approximated by Gaussian fits, the extent is not well defined. Instead, receptive field overlap was analyzed using the normalized nearest neighbor distance (NNND). For a given cell, the NNND is given by $2R/(\sigma_1 + \sigma_2)$, where R is the distance between the Gaussian fit center points of each cell and its nearest neighbor in the mosaic, and σ_1, σ_2 are SDs of the fits measured along the line connecting the center points. Thus, for nearest neighbors that exactly touch at the 1 SD boundary, the NNND is 2. Note that the NNND is large when overlap is small, and vice-versa. This representation has the advantages of being closely related to a standard anatomical measure (NND) and allowing for unbiased comparison of overlap in cell types with different absolute sizes.

A control analysis verified that the estimate of the NNND was not affected by different pixel sizes. In one preparation, RFs were measured using several pixel sizes (96, 60, and 18 μm per pixel), and the NNND was computed for the ON and OFF parasol cells and ON midget cells. Within each cell type, the modal NNND value varied by less than 12% across the three pixel sizes, demonstrating that pixel size did not significantly affect the NNND.

2.4.5 RF Profiles

The average RF profile of neighboring cells was computed separately for each mosaic in several steps. First, the spatial part of the RF was obtained by applying singular value decomposition to STA frames where the contrast intensity was at least 20% of the peak contrast. These were usually the frames approximately 80 to 30 milliseconds before the spike. Second, the center point of each spatial RF was estimated by taking the center of mass of all pixels with amplitude at least half that of the highest amplitude pixel. Third, the amplitude of each STA was scaled so that the central region of the STA had unit variance. The central region was the circle centered on the center of mass with a radius of 3 times the nearest neighbor spacing. Fourth, the line connecting each cell to its nearest neighbor was

computed. Along this line, absolute distance was normalized so that the nearest neighbor was exactly 1 unit away. Fifth, the RF amplitude of the reference cell and its nearest neighbor at each pixel along the nearest neighbor line were extracted. Thus the RF intensity was a continuously valued function with a staircase shape representing the distinct pixels in the RF. Finally, the RF profiles were averaged for each reference cell. The amplitude was normalized so that the variance over the range shown in Figure 2.3 had unit variance.

2.5 Acknowledgements

Chapter 2, in full, has been submitted for publication of the material as it may appear in Neuron, 2008, Gauthier, Jeffrey L; Field, Greg D; Sher, Alexander; Greschner, Martin; Shlens, Jonathon; Litke, Alan M; and Chichilnisky, Eduardo J, Cell Press, 2008. The dissertation author and Greg D Field were the primary investigators and authors of this paper.

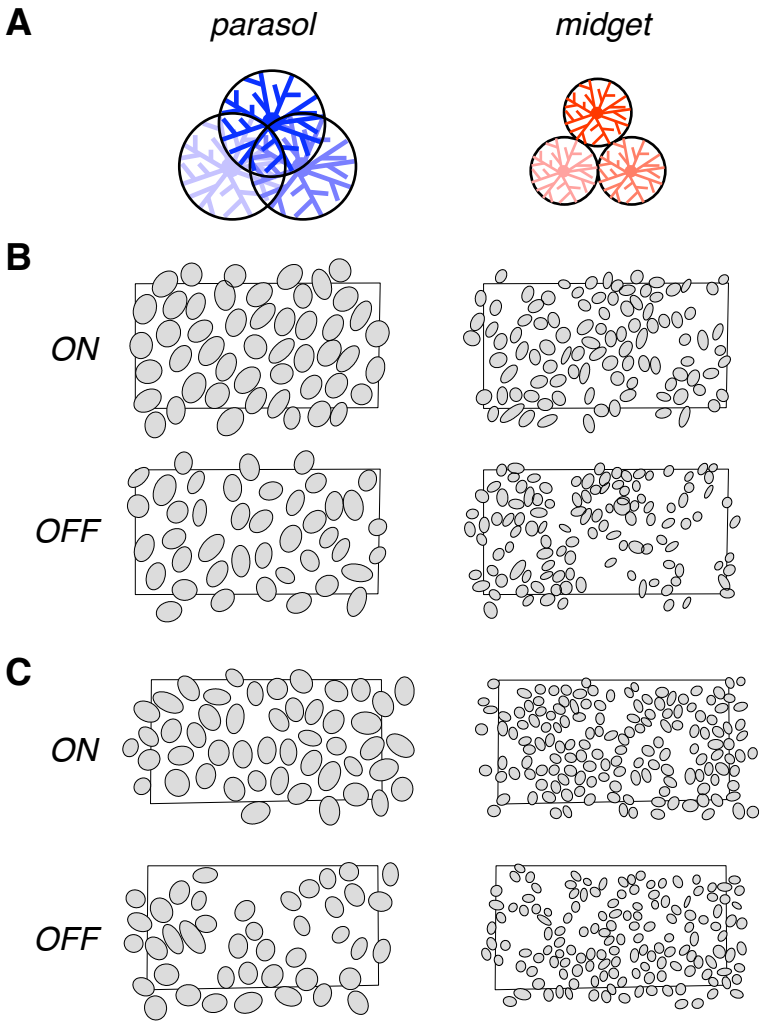

Figure 2.1: Parasol and midget RF mosaics and anatomical prediction. ***A.*** Previous anatomical findings indicate that parasol cell dendritic fields overlap substantially, with the tips of each dendritic field reaching the soma of its neighbors in the mosaic, while midget cell dendritic fields abut at their boundaries. ***B.*** Each panel shows the RFs of simultaneously recorded ON and OFF parasol and midget cells from one retina, with each RF represented as the 1 standard deviation boundary of a Gaussian fit to the RF center. Black rectangles indicate the outline of recording array (1800 by 900 micrometers). Gaps in the mosaic probably represent unrecorded cells. Retinal temporal equivalent eccentricity: 6.4 mm. ***C.*** Same as in B for a second preparation (temporal equivalent eccentricity 9.0 mm).

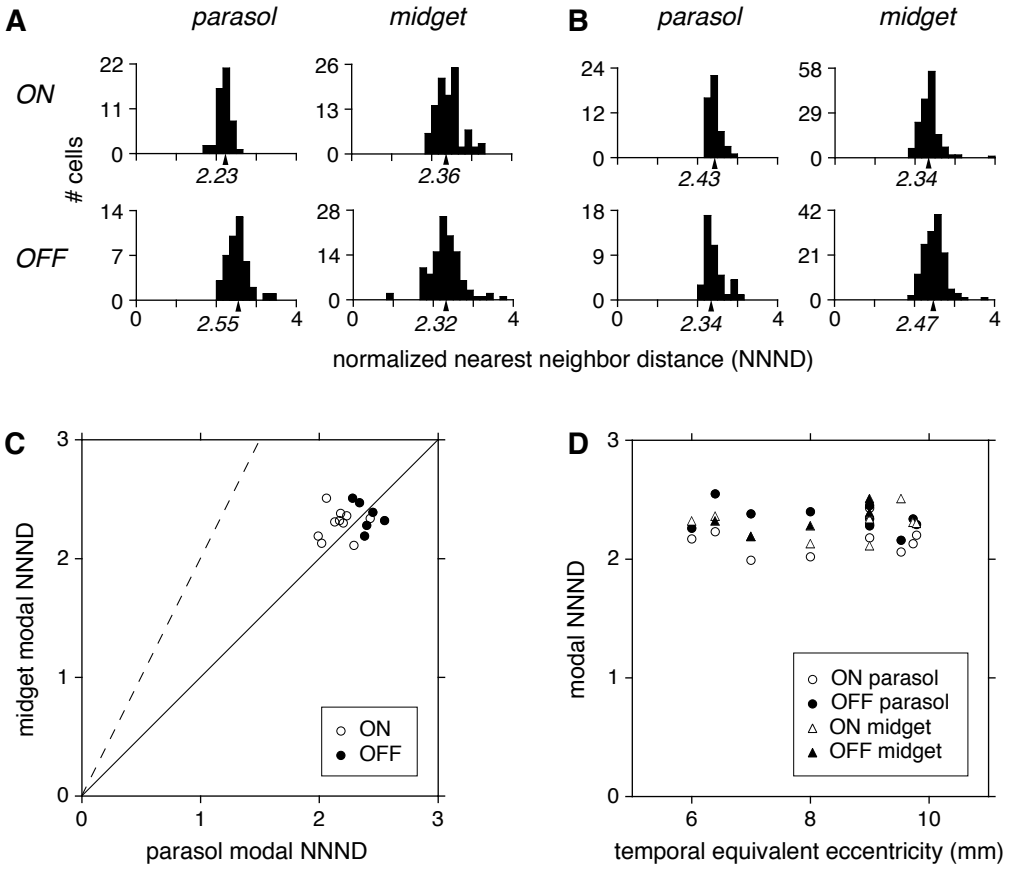

Figure 2.2: Quantitative analysis of RF overlap. The normalized nearest neighbor distance (NNND) measures RF spacing relative to RF size; if two mosaics have the same degree of RF overlap, they will have the same NNND. ***A.*** NNND values for the mosaics of parasol and midget cells shown in Figure 3.2B, with the modal NNND (mean of the densest 75% of values) indicated on the abscissa. Because the recordings did not sample every cell in the mosaic, the modal NNND was computed in a way that excluded outlying points, and the robustness of this calculation was confirmed by subsampling analysis (see Methods). ***B.*** Similar data, for the preparation in Figure 3.2C. ***C.*** Data summarizing the RF overlap of 36 mosaics (3,221 cells spanning 10 preparations). Modal NNND values of simultaneously recorded parasol and midget mosaics are compared separately for ON cells (open circles) and OFF cells (filled circles). Solid line indicates equality, dashed line indicates the prediction from anatomical findings that NNND should be twice as large for midget cells. ***D.*** NNND values as a function of retinal eccentricity, for ON (open) and OFF (filled) cells of both midget (triangle) and parasol (circle) types.

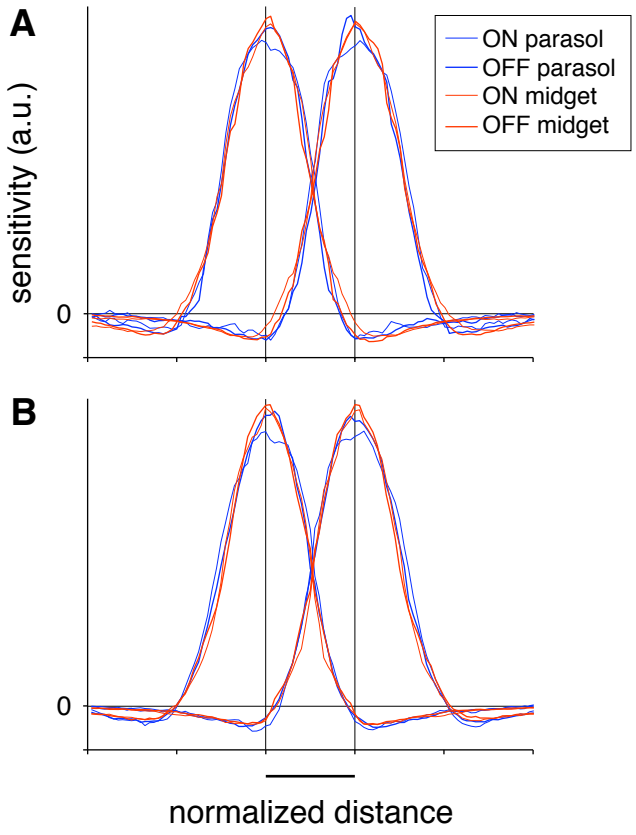

Figure 2.3: Nearest neighbor RF profiles for ON and OFF parasol and midget cells. ***A.*** For each cell type, the average RF profiles of a cell and its nearest neighbor were computed directly by interpolation of the spatial receptive field (see Methods). Distance and amplitude were normalized to focus on the RF profile shape independently of absolute size, spacing, and sensitivity. Distance was normalized for each pair of nearest neighbors (see Methods), and the scale bar at bottom indicates the distance between nearest neighbors. Sensitivity was normalized to have the same variance across cell types (see Methods). Data are from the preparation shown in Figure 3.2C. ***B.*** Same as A, from a second preparation (temporal equivalent eccentricity 9 mm).

Chapter 3

Receptive Field Interlocking

In the early visual system, large ensembles of neurons collectively sample visual space with receptive fields (RFs). A puzzling problem is how neural ensembles provide a uniform, high-resolution visual representation, in spite of irregularities in individual RFs. We approached this problem by simultaneously mapping the RFs of hundreds of primate retinal ganglion cells. Surprisingly, the irregular shapes of RFs were coordinated at an exquisite resolution: RFs interdigitated with their neighbors, filling in gaps and avoiding overlap which would otherwise degrade the collective representation. The coordinated irregular features could not be explained by standard Gaussian models, demonstrating that irregularities appearing to be "noise" in individual cells are in fact critical for covering visual space. RF shapes were coordinated with high spatial precision: the observed uniformity was degraded by angular perturbations as small as 15 degrees, and the observed populations sampled with more than 50% of the theoretical ideal uniformity. Thus the primate retina encodes the visual scene using an exquisitely coordinated collective representation, a remarkable feat given the multiple layers of circuitry involved, with important implications for neural development and downstream processing. These observations also indicate that the nervous system employs a greater degree of functional precision than previously appreciated.

3.1 Introduction

In primates, high resolution visual information is encoded by the magnocellular and parvocellular pathways, which respectively originate in the retina as populations of parasol and midget retinal ganglion cells [48]. These cells are expected to represent the visual scene efficiently and completely. Contrary to this expectation, indirect evidence suggests that the receptive fields (RFs) of individual parasol and midget cells have irregular and inconsistent shapes [60, 14–16], and thus that the visual representation is patchy, with inhomogeneous gaps and overlaps [15]. The problem of uniformly sampling visual space has an intriguing conceptual correlate, and potential solution, in the anatomical literature: in some ganglion cell types, dendritic fields (DFs) are coordinated to more uniformly cover the physical surface of the retina [61, 62, 28]. However, coordination of DFs seemed unlikely to produce coordination between RFs because, despite a rough alignment, RF shapes do not consistently match DF shapes at fine spatial scale [38, 39, 14, 15]. Moreover, the DFs of primate parasol cells do not exhibit any obvious coordination [26]. We therefore set out to test whether and how ganglion cells in the high resolution visual pathways are coordinated to transmit a uniformly sampled image to the brain.

3.2 Results

To measure directly how ganglion cell populations sample visual space, we exploited a novel recording technology: large-scale simultaneous recordings from hundreds of identified neurons in patches of peripheral primate retina [32, 33]. Stable recordings spanning multiple hours allowed RFs to be mapped at fine spatial scale. Because hundreds of cells were recorded simultaneously, cells could be grouped into clear functional classes defined by physiological properties such as latency, light response polarity, and spike train autocorrelation (see Methods) [34, 33, 35]. These properties, combined with the density of each functional class, definitively identified the ON- and OFF-parasol and ON- and OFF-midget cells, distinct anatomically defined populations with distinct projection patterns in the brain. Frequently ev-

ery cell of a type was recorded in a local region, presenting a unique opportunity for the study of collective encoding.

Parasol and midget cells RF shapes strongly deviated from the common theoretical ideal of a smooth surface defined by a difference of Gaussians [36,60,15,16,34]. Instead, RF shapes exhibited fine structure and irregular outlines, with shapes and sizes varying significantly from cell to cell (Fig. 3.1a-e). The observed irregularity of individual RFs suggested that the collective visual coverage by each cell type might also be uneven and irregular, potentially posing a major problem for high-resolution vision.

Examination of the entire population, however, revealed an elegant resolution to the problem of irregular RF shapes: RFs interlocked to sample visual space more uniformly (Figs. 3.1f, 3.2). To visualize the collective arrangement of RF shapes, each RF was summarized by interpolating a contour line at a single sensitivity level, similar to an iso-elevation line on a topographical map. The contour lines for all RFs of a single class were then plotted together to illustrate the collective visual sampling. The locations of RFs of each class formed an approximately regularly spaced lattice (Figs. 3.1f, 3.2), as observed in previous anatomical and physiological studies [26, 28, 34, 33]. Surprisingly, however, RFs showed a striking tendency toward coordinated structure: irregular outlines of neighboring cells complemented each other, interdigitating like jigsaw puzzle pieces. RFs were coordinated in a highly precise fashion in all four major cell types (Fig. 3.2). There appeared to be no coordination between cells of different types (not shown), emphasizing the importance of clearly distinguishing one cell type from another when studying the encoding of a neural population.

The observed coordination of RFs produced more uniform visual sampling than expected by chance, as demonstrated using a geometric test. The null hypothesis was that visual sampling was no more uniform than expected from random interaction between irregular RF shapes, where "irregular RF shapes" were defined as deviations from circular symmetry. Under this null hypothesis, mirroring each RF around its center point would not impact uniformity. To test this hypothesis, the arrangement of simultaneously recorded RFs of a single type (Fig.

3.3a, first column) was compared to the arrangement obtained after each RF was artificially mirrored (Fig. 3.3a, second column). Visual inspection showed that mirroring severely disrupted visual coverage: the area covered by exactly one RF contour (gray) was significantly reduced, and there were many more gaps (black) and overlaps (white). Thus RF shapes are not arranged randomly, but rather are coordinated in a way that provides more uniform coverage of visual space.

The spatial features of RFs that are important for uniform visual coverage were not captured by the most accurate theoretical RF model, an elliptical difference of Gaussians [63, 16, 34]. This was demonstrated using a second test in which the null hypothesis was that deviations from elliptical symmetry did not produce more uniform coverage. The hypothesis was tested by rotating each RF by 180° around its center point, a perturbation which left the overall elliptical shape intact but broke up any coordination between the non-elliptical structure of adjacent cells. Rotating each RF substantially disrupted coverage (Fig. 3.3a, first and third columns), rejecting the null hypothesis. Thus, although RF shapes exhibit "noisy" deviations from smooth elliptical models, the deviations are critical for the population to sample visual space uniformly.

The above observations were confirmed quantitatively using a numerical measure of the regularity of visual coverage: the uniformity index (UI, Fig. 3.3b). For a collection of RFs represented by a single contour level, the UI is the proportion of visual space covered by exactly one contour, computed only in regions where all cells seemed to have been recorded (see Methods). Graphically, the UI is the fraction of space in Figure 3.3a that is colored gray. Higher UI values indicate more even coverage; if RF shapes interlocked perfectly, the UI would equal 1. Scatter plots in Figure 3.3b show that the UI is significantly reduced when RFs are mirrored or rotated by 180°, confirming statistically the visual inspection of perturbed RFs. This result was not affected when the threshold level defining RF contours was moved by as much as 50% above or below its optimal value.

The striking coordination of RF structure suggested that retinal circuits may sample the visual scene with high precision, perhaps in a manner that approaches the optimum for high resolution vision. To measure the precision of interdigitation,

RFs were artificially perturbed, and the minimal perturbation that significantly disrupted visual coverage was identified (Fig. 3.4a-d). When RF shapes were simultaneously rotated around their respective center points, a rotation as small as 15 degrees led to a significant reduction in the UI. The minimal angle was similar for both parasol and midget cells, showing that in both populations the arrangement of RF shapes is exquisitely tuned to sample visual space more evenly. The UI was also used to characterize the degree to which cell to cell variability contributed to uniform coverage. When each RF in the observed population was replaced with the average RF, the UI was substantially lower (Fig. 3.4e, "observed" vs "average RF"). This observation suggests that uniform sampling is more important for visual encoding than stereotyped RF shapes.

The observed RFs approached an optimal arrangement, as demonstrated by comparing the UIs of various simulated populations. RFs are commonly modeled as a hexagonal lattice of identical circular difference of Gaussians functions [64–66]. Because of regular spacing and regular shapes, this idealization produces a very uniform sampling (Fig. 3.4e, "Gaussians on a hexagonal lattice"). But when the smooth ideal RFs are replaced with the observed irregular and variable RFs, uniformity drops substantially (Fig. 3.4e, "RFs on hexagonal lattice"); when RFs are located on the observed quasi-regular lattice, uniformity falls even further (Fig. 3.4e, "scrambled RFs"). This observation confirms the prediction that irregular RF shapes, when not coordinated, degrade the uniformity of visual sampling [15]. With coordination, however, uniformity increases dramatically. Compared to the baseline of uncoordinated RFs (Fig. 3.4e, "scrambled RFs"), the observed RFs exhibited uniformity 53% of the optimum given by perfectly interlocking shapes (Fig. 3.4e, "interlocking polygons"). Thus, the coordination of retinal RFs produces a substantially more uniform visual representation than would occur if RFs were independently formed.

3.3 Discussion

The present results demonstrate that the primate retina employs a finely-coordinated population code to achieve an efficient and complete representation of visual space. This finding has several important implications for retinal circuitry, retinal development, and the broad understanding of neural population codes.

What retinal mechanisms precisely coordinate RF shapes? As discussed above, ganglion cell DFs seem not to determine the fine contours of RF shape. Therefore precise coordination of RF shapes seems likely to involve the layers of circuitry that connect light sensitive cones to ganglion cells [67]. For example, the regular lattice of bipolar cells might contact ganglion cells in a partly exclusive fashion, so that two neighboring ganglion cells would not both receive strong input from the same bipolar cell [68, 69]. This hypothesis is supported by the finding that the spatial arrangement of bipolar cell synapses onto ganglion cells is highly variable [70, 41], consistent with each ganglion cell requiring a unique pattern of bipolar cell inputs to achieve coordination with its neighbors. Alternatively, inhibitory amacrine cell inputs might reduce the sensitivity of RF lobes that would otherwise jut too far into a neighboring RF [71]. In either case, the discovery of coordination between RF shapes provides a guiding framework for understanding the many retinal circuit elements that determine the fine features of RF shape.

How might RF shape coordination arise during development? Given the diversity of circuit elements that must be arranged to precisely align interlocking RF shapes, one possibility is that RF shapes arise from plasticity driven by visual input [57, 55]. Under this hypothesis, the mechanisms which modify retinal circuitry would be sensitive to the functional overlap of ganglion cell RFs, as distinct from anatomical growth cues or patterns of spontaneous activity [72]. It will be interesting for future studies to test this hypothesis by investigating how early in development RF shapes appear to be coordinated and how the coordination is affected by rearing in light- or form-deprived visual environments [56].

The present results have surprising implications for how populations of neurons produce an efficient and complete representation. Recorded in isolation, single neurons frequently exhibit highly irregular features, suggesting that large populations

must rely heavily on averaging or interpolation to produce accurate sensory performance or behavior (e.g. see [73–75]). The present results, however, show that in a complete population irregular features can be integral to a finely coordinated population code. This suggests that the nervous system operates with a much higher degree of precision than previously anticipated, and that irregularities of individual cells may actually reflect an unappreciated aspect of neural organization (e.g. [76]).

3.4 Methods

3.4.1 Summary.

In accordance with institutional guidelines, retinas were obtained from deeply anesthetized monkeys (*macaca mulatta, macaca fascicularis*) being euthanized for other experimental procedures, as described previously [35]. For recording, patches of peripheral retina 3-5 mm in diameter and 6-12 mm from the fovea were isolated from the pigment epithelium and held flat against a planar array of 512 extracellular recording electrodes. The preparation was perfused with oxygenated and bicarbonate-buffered AMES medium (Sigma, pH 7.4, 32-35°C). The visual stimulus was produced using the optically reduced image of a computer monitor focused on the photoreceptors. Voltage data for each electrode was digitized at 20KHz. Offline, spike waveforms were sorted into clusters in a multistep procedure [35], and clusters with a minimum refractory period between spikes were identified as single neurons. All computer analyses were performed using custom software.

RFs were mapped by computing the spike-triggered average (STA) stimulus obtained in the presence of a white noise stimulus. Features of the STA were parameterized using a separable model consisting of a spatial 2D difference of Gaussians, a biphasic timecourse, and a spectral profile. For analysis of RF shape, the spatial component of the STA was extracted using singular value decomposition across time. Light sensitivity was normalized across neurons by regressing the RF to match an elliptical single Gaussian fit with a peak of 1. After spatial smoothing with a low pass filter (typically r = 0.3 to 0.9 pixels), contour lines were linearly

interpolated in each RF. The contour level was the same for all RFs in a functional class and was selected to maximize the UI. The UI was equal to the proportion of space covered by exactly one contour (excluding both gaps and overlaps). It was computed only within the area in which all cells appeared to have been recorded, as defined by an automated procedure (see below).

Simulated RFs were defined in spatial bins the same size as the pixels of the measured RFs, and independent Gaussian noise was added to each bin to match the noise in measured RFs. For reshuffling of measured RFs, each RF was translated to its new location without additional noise. The UI of simulated RFs was computed using the same procedure as for the measured RFs.

3.4.2 Tissue Preparation.

Eyes were enucleated and hemisected and the vitreous was removed in room light, as described previously [35]. Retinas remained attached to the pigment epithelium and incubated in the dark for at least 30 minutes prior to recording.

3.4.3 RF Characterization.

Within each pixel of the flickering checkerboard stimulus, the red, green, and blue monitor guns were modulated based on random draws from a binary distribution, chosen independently in space and time. Pixel sidelengths ranged from 18 to 60 microns, and the color changed every 8 to 50 msec. For each neuron, the spatiotemporal RF was estimated by computing the average stimulus over the 250 ms preceding a spike. This RF included the contribution of both center and surround. Although the surround timecourse was delayed compared to the center timecourse, the stimulus update temporal period was sufficiently long that this delay did not significantly impact the spatial RF estimate.

3.4.4 The Uniformity Index.

The UI was computed over a region in which all cells appeared to have been recorded, as defined by an automated procedure. First, the Delaunay triangulation

[77,35] was applied to the collection of Gaussian fit center points. The area for the UI computation included only those Delaunay triangles defined by three pairs of "neighboring" RFs; a pair of RFs were considered "neighbors" if they were closer than 1.9 times the median nearest neighbor distance. This distance was chosen to match the results of a manual procedure.

Within each Delaunay triangle, a "local UI" was computed as the area covered by exactly one cell within the triangle. The reported UI for the whole population was computed across the area occupied by all triangles. Error bars were equal to the standard error of the mean (SEM) of a subset of the local UIs. The subset was chosen so that no two triangles shared an edge, ensuring that local correlations in the UI did not artificially reduce the SEM. The same subset of triangles was used to compare whether two conditions were significantly different (e.g. observed RFs compared to mirrored RFs).

The SEM and statistical tests described above were validated using a bootstrap simulation. The simulation concluded that the SEM was a conservative estimate, typically overestimating the standard deviation of the UI by 30 to 60%. It also concluded that the statistical tests were conservative, with $p<0.05$ in 0.5-3.0% of comparisons.

3.4.5 Rotation Plot (Fig. 3.4a-d).

Each RF was rotated about its center point by the same angle, and for each such rotation the contour level was chosen to maximize the UI. After generating rotated contours, the following procedure was applied to each cell type. First, data was pooled from all preparations in which sufficiently many cells of that type were recorded. A subset of the Delaunay triangles was chosen in each preparation as described above, and the "local UI" values of these triangles were averaged from all datasets to determine the mean UI at each rotation angle (including 0), with error bars equal to the SEM. For each nonzero rotation angle, a one-tailed two-sample t-test determined whether the UI was significantly lower ($p<0.01$) than the UI of the unrotated RFs.

3.4.6 Generation of Simulated RFs.

Mirror test: each RF was mirrored about an axis passing through the Gaussian fit center point. The angle of the mirror axis was chosen using a procedure that ensured it was both arbitrary and unique. For visualization (Fig. 3.3a), the axis was parallel to the short edge of the boundary of the region shown. For quantitative analysis (Fig. 3.3b), the axis was parallel to the short edge of the recording array.

Interlocking polygons: Voronoi domains were computed based on the center points of measured RFs. Each RF was shaped like the Voronoi domain with amplitude following a Gaussian taper matched to the taper of the observed RFs.

Gaussians on a hexagonal lattice: Lattice spacing was equal to the median nearest neighbor spacing of the measured RFs. Each RF was a circular difference of Gaussians dome with center radius equal to 0.5 times the lattice spacing, surround radius equal to twice the center radius, and surround amplitude equal to 0.2 times the center amplitude.

RFs on a hexagonal lattice: cell centers were located on a regular hexagonal lattice, and the cell at each location was a randomly chosen RF from the original population.

Average RF: each RF was replaced by the average RF with noise added to match the noise in observed RFs.

Scrambled RFs: each RF was replaced by a randomly chosen RF from the same preparation. The lattice of RF center locations was held constant.

3.5 Acknowledgements

Chapter 3, in full, has been submitted for publication of the material as it may appear in PLoS-Biology, 2008, Gauthier, Jeffrey L; Field, Greg D; Sher, Alexander; Greschner, Martin; Shlens, Jonathon; Litke, Alan M; and Chichilnisky, Eduardo J. The dissertation author was the primary investigator and author of this paper.

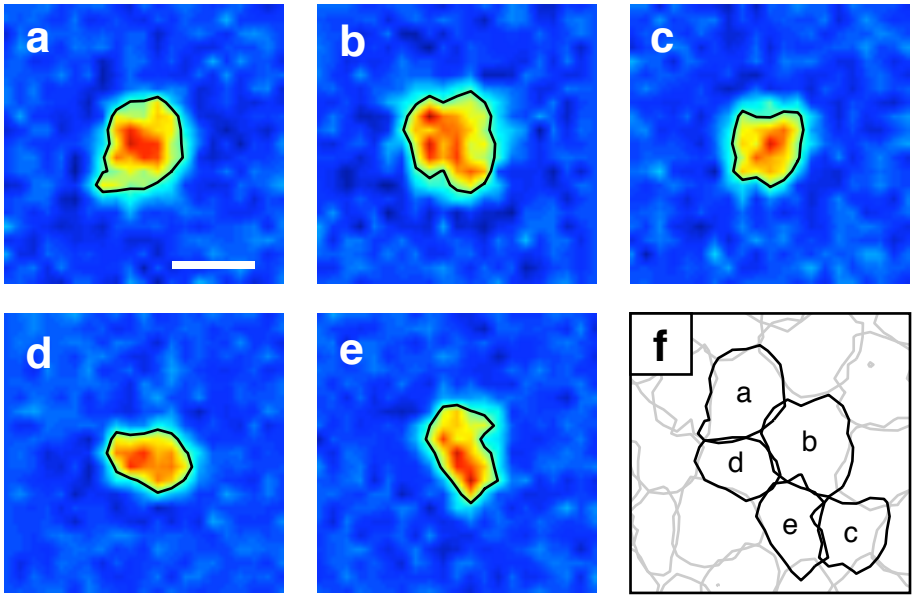

Figure 3.1: RFs have irregular and variable shapes that deviate from smooth models. a-e. Receptive fields (RFs) of five simultaneously recorded ON-parasol cells mapped by white noise reveal irregular fine structure which deviates from a simple Gaussian model. Warmer colors indicate greater light sensitivity. For visualization (Figs. 1 and 2) and analysis (Figs. 3 and 4), each RF was low pass filtered to reduce measurement noise and summarized by a contour line describing its shape at a single sensitivity level (see Methods). Surrounds were too weak to be seen in individual cells, but averaging over cells showed a clear but shallow surround in all four cell types (data not shown). The RFs of OFF-parasol and ON- and OFF-midget cells had similar irregular shapes (contours shown in Fig. 2b-d). For visualization in this figure only, pixels were sub-sampled with linear interpolation by a linear factor of 3. Scale bar is 120 micrometers. **f.** The contours of the ON-parasol cells shown in panels a-e. RF shapes interlocked to sample visual space more uniformly.

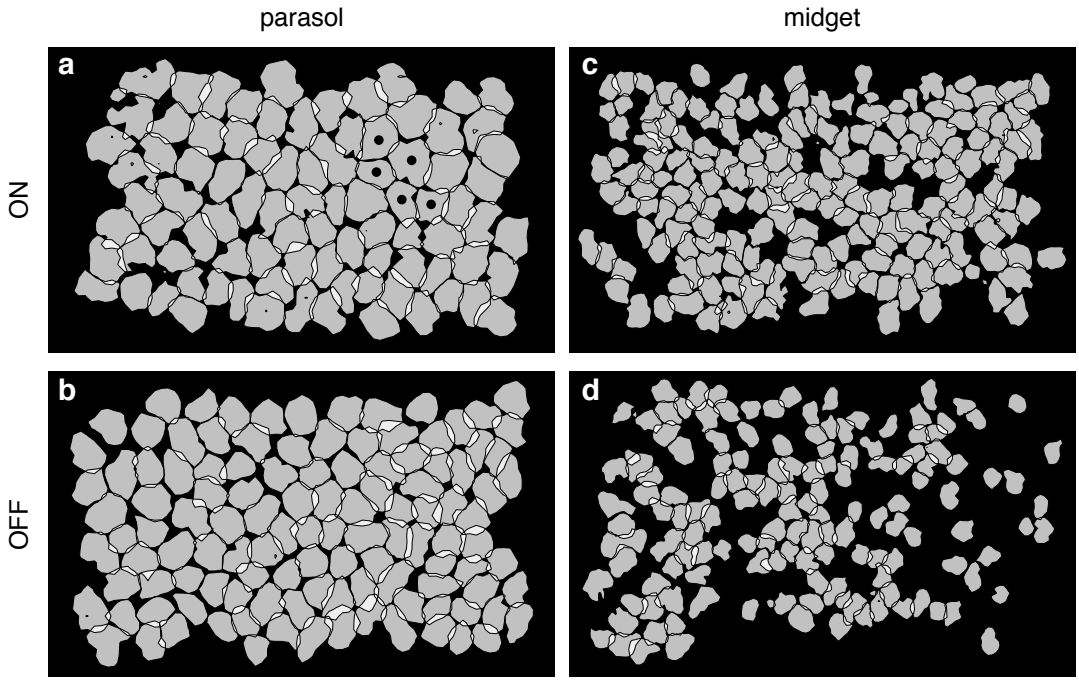

Figure 3.2: Irregular RF shapes interlock to provide more even coverage of visual space. The simultaneously recorded RFs of each cell type formed a regularly spaced mosaic, represented here as a collection of contour lines. The contour level was the same for all cells in a mosaic, chosen so that neighboring cells tended to just touch (see Methods). The width of each panel is 1.8 millimeters. **a.** RFs of 88 simultaneously recorded ON-parasol cells from 9 mm eccentricity (temporal). Cells marked with a dot are those shown in Figure 1. **b.** RFs of 117 simultaneously recorded OFF-parasol cells from the same preparation as in panel a. **c.** RFs of 179 simultaneously recorded ON-midget cells from 8 mm eccentricity (superior). Gaps are presumably due to some cells not being recorded. **d.** RFs of 141 simultaneously recorded OFF-midget cells from 11.5 mm eccentricity (superior-nasal).

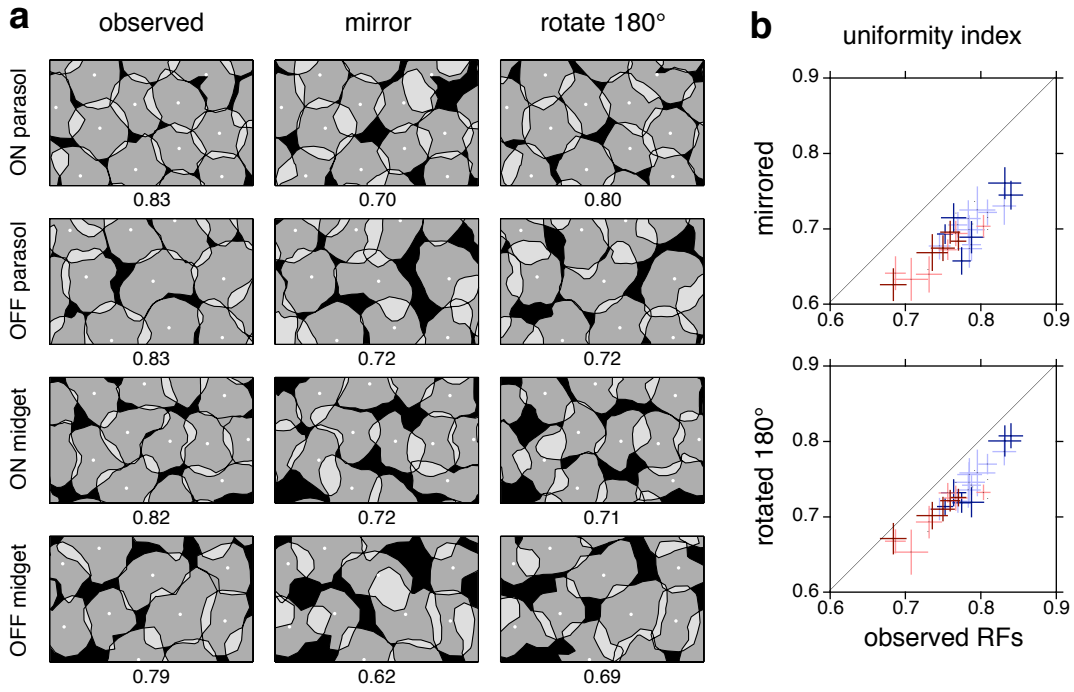

Figure 3.3: RF shapes are coordinated to make coverage more even, and deviations from elliptical Gaussian models are important for coordination. a. Simultaneously recorded populations of ganglion cell RFs shown at high resolution, and visual tests of RF interdigitation. In the observed mosaic (left column), cells appeared to interlock like puzzle pieces. Randomizing the interaction between RF contours by mirroring (center column) or rotating (right column) disrupted visual coverage, demonstrating that fine RF structure interacts locally to make visual coverage more uniform (see text). The center point around which RF contours were rotated or mirrored was the center point of an elliptical difference of Gaussians fit. Numbers beneath each panel indicate the uniformity index (UI) in this region (see text). The respective horizontal widths of panels for each cell type are 155, 140, 95, and 55 micrometers. **b.** Statistical tests demonstrate that RF interdigitation is highly significant across many preparations. For each population of simultaneously recorded cells of a single type, the UI value is compared between the observed data and when RFs were mirrored or rotated (see text). ON-parasol data are shown in light blue, OFF-parasol in dark blue, ON-midget in light red, OFF-midget in dark red. In every population, the UI decreased when RF contours were perturbed, demonstrating that fine RF structure is coordinated with neighbors to enhance visual coverage. Each population was composed of 34 to 239 (mean 98) simultaneously recorded cells, for a total of 3,140 cells from 32 populations. Error bars are the standard error of the mean within each population (see Methods).

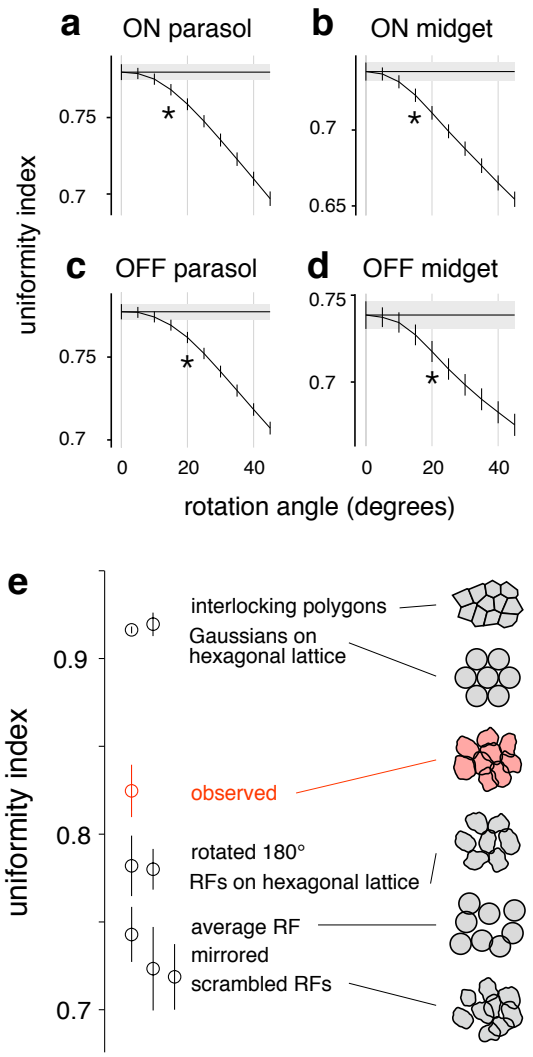

Figure 3.4: RF shapes are coordinated with high precision and their arrangement approaches optimal uniformity. a. Test to identify the minimum perturbation that significantly disrupts the uniformity of coverage. For ON-parasol preparations, the UI is plotted as a function of the angle by which RFs were rotated around their center points. Data from clockwise and counter-clockwise rotations were pooled (see Methods). An angle as small as 15 degrees significantly reduced the UI ($p<0.01$), and this angle is represented as an asterisk beneath the curve. Horizontal black line and gray rectangle indicate the mean and error bars on the unrotated condition. **b-d.** Same analysis as in Fig. 4a applied to other cell types. **e.** UI values of observed RFs and various simulated RFs from a representative population of ON-parasol cells. In the simulated RFs, noise was added to match the measurement noise in the observed RFs (see Methods). For interpretation, see text.

Chapter 4

Single Cone Inputs

4.1 Introduction

Multiple layers of retinal neurons transform the photon catch of rods and cones into the spiking activity of ganglion cells. Although each layer of retinal processing has been studied in isolation, no technique has permitted describing the complete retinal transformation, i.e. measuring how a lattice of ganglion cells samples from the lattice of photoreceptors. Indeed, nowhere in any modality has an intermediate sensory representation been fully characterized in terms of fundamental receptors.

Precisely characterizing the sampling of ganglion cells is especially important in visual pathways with high spatial resolution. In primates, the limits of acuity across the visual field are set by the density of midget ganglion cells, not by the density of cones [17]. Thus, characterizing how midget cells sample from individual cones is a prerequisite for understanding the neural encoding of high resolution visual information.

Specifically, it is unknown whether midget cells share cones, or if each cone provides exclusive input to only one midget cell. Populations of ON and OFF midget cells each form a regularly spaced mosaic [28]. Although the sizes and densities midget receptive fields (RFs) have been measured previously [22, 28, 30, 78], these measurements are too coarse to determine whether neighboring RFs in the mosaic overlap at the level of individual cones. Absent direct measurement, various predictions about midget RF overlap arise from previous anatomical and

physiological studies. Anatomically, midget cell dendritic fields (DFs) occupy non-overlapping territories, with neighboring DFs meeting at an intricate boundary [28]. This anatomical avoidance might suggest that midget cell RFs avoid sampling from the same cones. In addition, midget cell DFs exhibit another exclusive interaction that might suggest they avoid sharing cones: human midget DFs seem not to contact all the midget bipolar cells within their territory [28]. On the other hand, physiological measurements from midget bipolar cells found that a midget bipolar RF is slightly larger than the cell's anatomical extent [42]. It remains unknown, however, whether neighboring bipolar RFs are wide enough for neighboring midget cells to receive input from the same cones. It is also unknown whether midget RFs contain gaps because some bipolar cells are not sampled.

The study of single cone inputs has an important precedent: one study [79] has successfully measured the contribution of individual S cones to primate small bistratified cells (SBCs). The study capitalized on two unique features of S cones in the primate retina: S cones exhibit much wider spacing and a highly distinct spectral sensitivity compared to the more numerous L and M cones. Using a white noise stimulus with sufficiently small pixels, the study distinguished the contributions of individual S cone inputs to the excitatory RF centers of neighboring SBCs. Though pioneering, its technique of physiological cone isolation can not be directly copied to identify L and M cone inputs to midget cells. First, L and M cones are more closely spaced and require smaller pixels to be used. Second, looking for gaps in midget RFs requires aligning anatomical cones locations with a physiological measurement to verify that no cones were missed.

Based partly on the methods of this study, we here introduce a new technique for directly measuring the single L and M cone input to midget cells in peripheral primate retina. The technique combines large-scale simultaneous recording of hundreds of ganglion cells, fine grained spatial maps of RF sensitivity, and anatomical localization of individual cones. Registering the functional and anatomical maps confirms that the RFs reveal single cone inputs to ganglion cells. These data show that midget cell RFs do not exhibit gaps, and that cones are in fact shared by neighboring midget cells.

4.2 Results

4.2.1 Fine RFs reveal single cone inputs

To measure the single cone inputs into midget ganglion cells, large-scale, simultaneous recordings were made from isolated pieces of primate retina. Recorded cells were sorted into functional groups based on physiological responses such as latency and polarity, and were identified as belonging to the anatomically defined classes parasol, midget, or SBC based on physiological responses and density (see Methods).

The receptive field of each ganglion cell was characterized using a spatial white noise stimulus (see Methods). In nearly all previous studies that employed white noise, pixels sizes were relatively large, with each pixel containing multiple photoreceptors [15,34]. In the present study, white noise pixels were made sufficiently small (approximately 6μm per side) that each pixel was predicted to overlay at most one L or M cone. Using these small pixels, individual RFs showed small islands of sensitivity, consistent with spatial isolation of individual cone inputs. Figure 4.1A shows one OFF midget cell RF recorded at 7 mm eccentricity (temporal retina, near horizontal meridian). The RF is shown as sensitivity to the green monitor gun (the strongest input to L and M cones) inverted and with contrast manually adjusted. Each bright island is a putative cone input.

To determine whether the islands of sensitivity corresponded to individual cone inputs, their locations were compared to an anatomical image of the cone mosaic. Because the retina was stimulated from the cone side, only cone outer segments were expected to exhibit light sensitivity. Cone outer segment locations were identified using two methods: a transmitted light image, and a fluorescent image using the semi-specific marker peanut agglutinin (PNA, [80]). The transmitted light image (Fig 4.1D) showed some cones clearly, but was not sufficiently clear to reveal all cones, nor could it distinguish inner and outer segments.

A much clearer image of anatomical cone locations was achieved with PNA labeling (Fig 4.1E). PNA revealed the locations of inner and outer segments, and also distinguished S cones from L and M cones (see Methods). A summary of cone

identities based on PNA labeling is shown in figure 4.1F: S cones are traced in blue, L/M cone inner segments in yellow, and L/M cone outer segments in red.

Comparing to anatomical cone locations confirmed that the islands of light sensitivity were in fact individual L and M cone outer segments. Anatomical cone locations were registered with RFs by displaying an alignment image on the stimulus monitor (Fig 4.1B, see Methods). Comparing a transmitted light image (Fig 4.1D) to a photograph of the alignment image projected onto the cones (Fig 4.1C) revealed the mapping between stimulus space and anatomical space. This allowed cone locations to be overlaid on the RF (Fig 4.1G). The comparison showed that each island of light sensitivity corresponded to a single L/M cone outer segment (red ellipses). As expected, there was no sensitivity at locations of inner segments (yellow ellipses). There was also no sensitivity at S cone locations because the RF shows only the green monitor gun, which does not strongly activate S cones. The blue monitor gun, which does strongly activate S cones, also showed no sensitivity (data not shown; for more on S cone input, see Discussion).

To demonstrate the alignment did not arise by chance, the RF was mirrored left-right (Fig 4.1H). In this image, there is no longer agreement between anatomical and physiological cone locations, confirming the validity of the original alignment, and thus confirming that the RFs revealed the contribution of single cone inputs. Similar results were found for two other nearby OFF midget cells (Fig 4.1I-L).

The observed midget RFs did not contain gaps. Examining the outline of each RF showed that all cones contained in the convex hull of the RF were sampled. While apparent "gaps" did seem to be present, comparison with anatomical cones reveals they were due to the presence of an S cone, or an irregularity in the spacing of the L/M cone mosaic.

4.2.2 Neighboring midget cells share cone inputs

Simultaneous recording of many cells allowed a direct measurement of whether L and M cones are shared among OFF midget cells. Figure 4.2A-C shows the RFs of the cells in Figures 4.1A, I, and K, plotted in a common coordinate space to facilitate comparing cone locations between cells. Figure 4.2D shows the superpo-

sition of the three RFs, with each false-colored red, green, or blue. Superposition demonstrated that these OFF midget cells did share cones with neighbors. White circles indicate which cones have significant input to more than one cell. Cells A and B share 1 cone and cells B and C share 2 cones, while cells A and C share no cones.

4.3 Discussion

The present results demonstrated that a fine white noise stimulus could reveal the single cone inputs to ganglion cell RFs. OFF midget RFs did not contain gaps, and simultaneous recordings from neighboring cells revealed that cones were shared in the local mosaic. The implications of these results and their relation to previous work are discussed.

4.3.1 Extent of midget cone sampling

Anatomical evidence in human retina makes the surprising suggestion that midget RFs might contain small gaps. Human midget DFs seem to not to contact all the midget bipolar cells within their DF territory [28], and these gaps were hypothesized to relate to specificity of L and M cone sampling. For example, a midget cell that sampled primarily from L cones might avoid bipolar cells connected to M cones.

The present results show that there are no gaps in midget RFs at 7 mm eccentricity, the same eccentricity at which anatomical avoidance was suggested. There are several possible explanations for the apparent mismatch. First, human midget cells might exhibit different connectivity patterns from those in the macaque. This seems unlikely, however, given the large number of observed similarities between the macaque and human midget pathways (e.g. [28]). Second, the anatomical measurement might not have labeled all segments of the midget DF. The anatomical study reported that the stains used, horseradish peroxidase and Neurobiotin, sometimes led to incomplete fills, and that incompletely filled cells were not analyzed. But if the criterion for judging completeness was not sufficiently strict,

the apparently patchy DF might in fact reflect an incomplete stain. Third, the lateral spread of functional connections in midget bipolar RFs might be sufficiently large to cover any gaps left by unconnected bipolar cells. Indeed, recordings from individual midget bipolar cells reveal that midget bipolar RFs are slightly larger than the corresponding DF [42]. If true, it would be surprising that a large number of midget bipolar cells do not contact midget ganglion cells, though contact with another ganglion cell type can not be ruled out. Future experiments will be required to distinguish these various possibilities.

Regarding the sampling of S cones, the absence of sensitivity to the blue gun (data not shown) does not conclusively demonstrate that S cones provide no input to OFF midget cells. Indeed, such input is suggested by anatomical connections [81], as well as preliminary results by the present authors (data not shown). The present recordings, however, are ambiguous on this point. S cones are among the least robust elements of the primate retina, and, in ex vivo recordings, S cones are typically the first cone type to become less sensitive due to bleaching. Therefore, to determine whether S cones provide input to a given RF, it is necessary to simultaneously record from a cell which samples S cones, such as an SBC [35]. Such a simultaneous recording serves to verify that the S cone in question is indeed functionally active. While the preparation shown here did include some SBCs, none overlapped the OFF midget cells shown. Therefore these data do not conclusively reveal whether or how strongly S cones are sampled by OFF midget cells.

4.3.2 Number of cones sampled by each midget cell

Previous studies have attempted to measure the number of cones feeding each midget cell using various techniques. One study [78] labeled midget cells with DiI or Neurobiotin injection, and counted the number of cones "underlying the dendritic field" of each midget. At 7mm eccentricity, counts ranged from 12 to 40 cones per midget cell. This large range is likely attributable to two sources of variability which were not controlled. First, the study did not distinguish ON and OFF cells, though ON cells are approximately 50% larger [27]. Second, it did not identify in which parts of the visual field cells were located, though DF

sizes at a fixed eccentricity can vary significantly in different quadrants [22]. Given these sources of uncertainty, it is difficult to compare these counts to the present measurements, or to use them to interpret the relationship between physiological and anatomical organization.

A more specific, though much more laborious, prediction of midget cone inputs comes from complete circuit reconstruction using electron microscopy (EM, [17]). The authors reconstructed the complete set of cones and midget bipolar cells directly connected to a midget ganglion cell at several eccentricities. An ON midget cell from 4 mm was found to receive input from 3 midget bipolars, each of which contacted 1 cone. An ON midget cell from 12 mm was found to receive input from 3 to 4 midget bipolars, each of which contacted 3 cones. Thus, assuming linear interpolation, an ON midget cell at 7 mm should have direct anatomical connections to 6 or 7 cones, and an OFF midget cell, such as the one shown in Figure 4.2, should contact 5 or 6 cones. The present physiological recordings show that each OFF midget makes strong functional connections to 9 to 12 cones. Thus, assuming accurate interpolation, OFF midget cells have functional contact with more cones than are contacted anatomically. This observation is consistent with the evidence that a midget bipolar cell receives functional input from more cones than are contacted directly [42]. It should be noted, however, that the EM reconstruction might have missed some midget bipolar inputs, so the counts are better interpreted as a lower bound on the number of anatomical connections.

4.3.3 Sharing of cones by individual midget ganglion cells

Previous studies have also made various predictions about how nearby midget cells sample from the mosaic of cones. The anatomical mosaics of ON and OFF midget cells each respectively tile retinal space without any overlap in their dendrites [28]. As described above, each cell seems to sample only a subset of midget bipolar cells within its dendritic territory [28]. These two observations suggest that neighboring midget cells receive input from a non-overlapping set of cones. In light of these anatomical results, it is surprising that neighboring midget RFs do share cones with nearby cells. This observation is consistent with the previous

findings, summarized above, that functional connections to the midget RF expand beyond the range of direct anatomical connections [42].

The observation of cone sharing also resolves ambiguity from previous coarse measurements. As described in chapter 2, midget RFs have a significant degree of overlap when measured using coarse pixels. While this finding suggests that midget RFs share cones, chapter 3 provides an alternative hypothesis: because RF shapes interlock on a fine scale, coarse measurements might mask exclusive cone contacts. Instead, the present measurements of single cone input reveal that individual cones can be strongly sampled by more than one midget RF.

The consequences of cone sharing for visual encoding are not well understood. Theoretical studies of Gaussian RFs suggest that functional overlap can serve various purposes (e.g. [45, 46, 82]). An important caveat is that these studies used a continuous approximation of the cone mosaic and smooth RFs, unlike the present case of a finite number of cones feeding irregularly shaped RFs. Thus it will be interesting for future studies to compare the cone sharing of midget and parasol cells to the predictions of theoretical models about how single cones should be sampled.

4.4 Methods

4.4.1 Physiological recording and RF characterization

Physiological recordings and RF characterization were performed as described in chapters 2 and 3, with the following exceptions. First, the size of stimulus pixels was much smaller (approximately 6μm per side): each stimulus pixel was one monitor pixel. Second, the stimulus update rate was 30Hz.

4.4.2 Cone labeling

Isolated pieces of retina were labeled with bath-applied lectin PNA conjugated to Alexa Fluor 488 (Invitrogen). A small amount of PNA (200μg) was added to approximately 10 mL of AMES medium in which the retina was prepared for

mounting on the recording array. The retina spent 5 to 10 minutes in this solution before being transferred to the array where it was perfused continuously with fresh AMES medium. Following several hours of physiological recording, PNA labeling was imaged in the living retina using a cooled CCD camera, a 10x objective, and a FITC filter cube.

4.4.3 Cone labeling and alignment

Anatomical images were aligned with RFs by projecting a frame of white noise onto the retina. In this frame, each pixel was either black or white with equal probability, and the pixel sidelength was approximately 12μm. An image of the white noise frame projected onto the retina (Figure 4.1C) was manually aligned with the white noise frame itself (Figure 4.1B). This alignment provided the mapping between physical coordinates and stimulus coordinates so that RFs could be overlaid on an anatomical image of the cones.

4.4.4 S cone identification

Following physiological recording, the retina was fixed for several hours in a solution of 4% paraformaldehyde in phosphate buffered saline. PNA labeling was imaged in the fixed retina with a confocal microscope using a 20x or 60x objective and a wide pinhole setting. Typically all cone pedicles could be seen in a single image plane. Some cone pedicles appeared brighter than others (Fig 4.3A-C), and the spacing of these bright pedicles matched the spacing of S cones in the cone mosaic. Bright pedicles were verified to belong to S cones by aligning them with a physiological map of blue light sensitivity. In one preparation, putative S cone locations were identified by aligning an image of cone pedicles (Fig 4.3C) with an image of cones in the living retina (Fig 4.3D). Putative S cone locations (Fig 4.3E, blue dots) were overlaid on a physiological map of S cone sensitivity (Fig 4.3E, gray pixels). The latter was the blue gun RF of a SBC, which has a distinctive S-ON, (L+M)-OFF response, and whose sensitivity to the blue monitor gun is a clear indication of S cone locations. The alignment between anatomical S cones and

functional S cone inputs (Fig 4.3E) confirmed that the bright pedicles belonged to S cones. It was also observed that S cones were more dimly labeled with PNA than L or M cones (Fig 4.3D), thus providing a means to identify S cones in the living retina without the need for additional tissue processing.

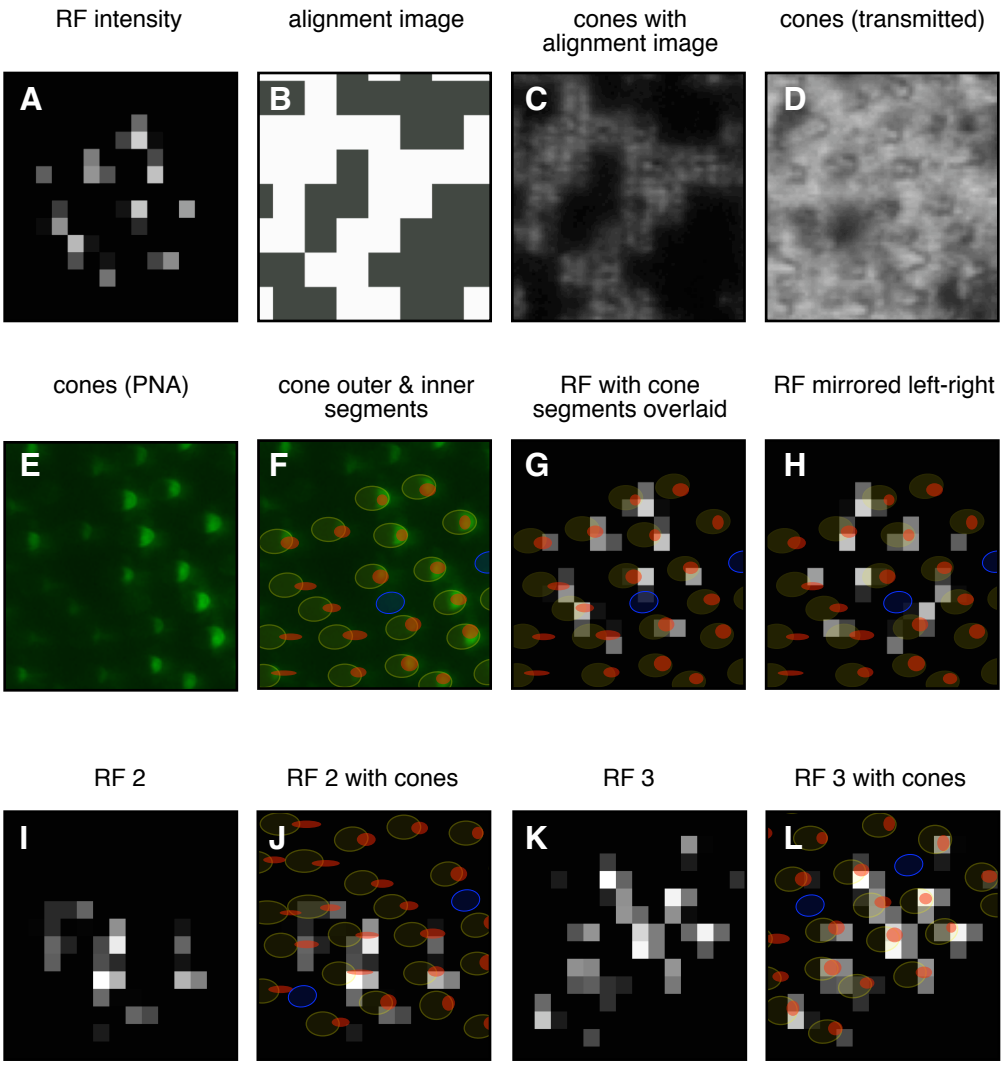

Figure 4.1: Alignment of single cone RF to anatomical cones. A. An OFF midget cell RF, with only sensitivity to the green monitor gun shown. Width is 90μm. **B.** Part of an image used to align stimulus space with anatomical images of the retina. **C.** Transmitted light image of the alignment image in B projected onto cones in the living retina. **D.** Transmitted light image of cones in the living retina. **E.** Fluorescent image of PNA staining. Bright spots are cone inner segments, faint smears are cone outer segments. **F.** Same image as E, with labels showing S cones (blue ovals), L/M cone inner segments (yellow), and L/M cone outer segments (red). **G.** Cone locations overlaid on the RF from A to show alignment between anatomical and physiological cones. **H.** Same as G, with the RF mirrored left-right. After mirroring, the anatomical and physiological cones no longer align, verifying the original alignment in G. **I,K.** Two other OFF midget RFs near the one shown in A. **J,K.** Same as G, for the RFs shown in I and J, respectively.

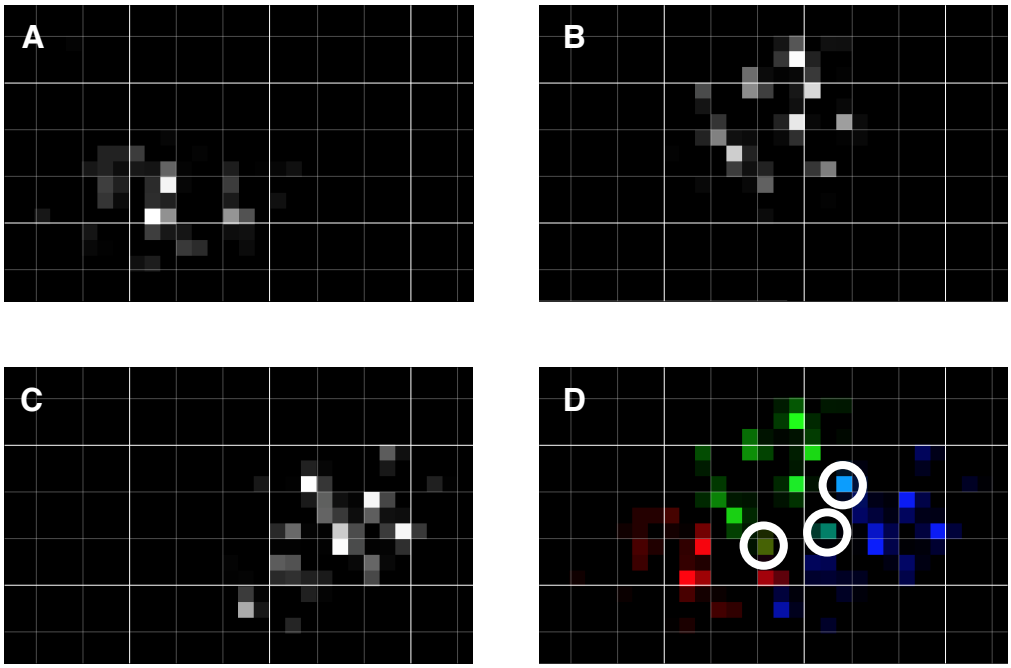

Figure 4.2: Shared cone sampling by three OFF midget cells. A-C. Three OFF midget RFs, also shown in Figures 4.1A, I, and K, respectively. Absolute coordinates are the same in each RF, with grid lines to facilitate comparing cone locations. Each large grid square is 80μm. **D.** Same three RFs, false colored and superimposed. White circles show shared cones.

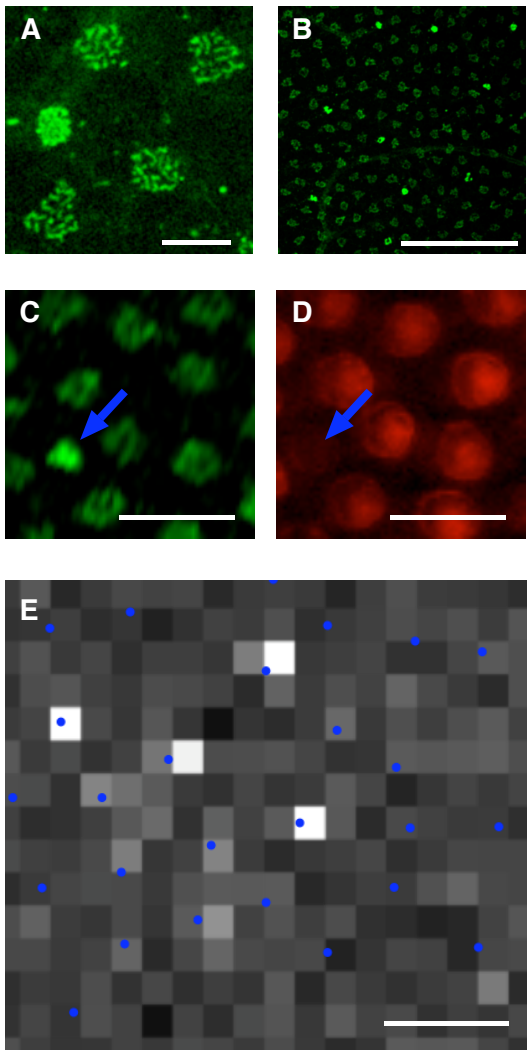

Figure 4.3: Identification of S cones. A. High magnification view of cone pedicles labeled with PNA. Brightly labeled pedicle is presumed to belong to an S cone. Scale bar is 10μm. **B.** Same as A, lower magnification. Bright pedicles have approximately the same spacing as S cones. Scale bar is 100μm. **C.** Same as in A. Blue arrow indicates a putative S cone pedicle. Scale bar is 20μm. **D.** Fluorescent image showing PNA labeling of cone inner and outer segments in living retina. Image shows the same cones whose pedicles are shown in C. Blue arrow points to the inner and outer segments of the cone with a brightly labeled pedicle in C. They are much more faintly labeled than in the surrounding cones. Scale bar is 20μm. **E.** Gray pixels are the RF of a SBC, with only blue monitor gun sensitivity shown. This image provides a physiological measure of S cone locations. Blue dots are locations of putative S cone inner/outer segments, identified as in C,D. Alignment between blue dots and white pixels confirms that brightly labeled pedicles belong to S cones. Scale bar is 100μm.

Chapter 5

Summary

This dissertation has explored several important aspects of how RGCs are organized at the population level. It has characterized the spatial sampling properties of local populations at progressively finer levels of detail, eventually reaching the elementary inputs to each RF. Chapter 2 demonstrated that the amount of gross RF overlap is indistinguishable in parasol and midget cell populations. Chapter 3 showed that individual RF shapes interlock to more uniformly cover the visual field. Finally, Chapter 4 revealed that midget RFs overlap even at the level of individual photoreceptors.

These findings describe novel aspects of population organization, perhaps the greatest unexplored conceptual territory in systems neurobiology. It is hoped that these studies will not only inform the understanding of retinal function, but also reveal themes and and inspire ideas that will be conceived and explored throughout the brain.

Works Cited

1. Gross C (2002) Genealogy of the "grandmother cell". Neuroscientist 8:512–518.

2. Best P, White A, Minai A (2001) Spatial processing in the brain: the activity of hippocampal place cells. Annu Rev Neurosci 24:459–486.

3. Ajemian R, Green A, Bullock D, Sergio L, Kalaska J, et al. (2008) Assessing the function of motor cortex: single-neuron models of how neural response is modulated by limb biomechanics. Neuron 58:414–428.

4. Britten K, Newsome W, Shadlen M, Celebrini S, Movshon J (1996) A relationship between behavioral choice and the visual responses of neurons in macaque mt. Vis Neurosci 13:87–100.

5. Butts D, Kanold P, Shatz C (2007) A burst-based "hebbian" learning rule at retinogeniculate synapses links retinal waves to activity-dependent refinement. PLoS Biol 5:e61.

6. Hartline H (1938) The response of single optic nerve fibers of the vertebrate eye to illumination of the retina. Am J Physiol 121:400–415.

7. Kuffler S (1953) Discharge patterns and functional organization of mammalian retina. J Neurophysiol 16:37–68.

8. Rodieck R (1998) The first steps in seeing. Sunderland, MA: Sinauer, 562 pp.

9. Wassle H, Riemann H (1978) The mosaic of nerve cells in the mammalian retina. Proc R Soc Lond B Biol Sci 200:441–461.

10. Peichl L, Wassle H (1979) Size, scatter and coverage of ganglion cell receptive field centres in the cat retina. J Physiol 291:117–141.

11. DeVries S, Baylor D (1997) Mosaic arrangement of ganglion cell receptive fields in rabbit retina. J Neurophysiol 78:2048–2060.

12. van Wyk M, Taylor W, Vaney D (2006) Local edge detectors: a substrate for fine spatial vision at low temporal frequencies in rabbit retina. J Neurosci 26:13250–13263.

13. Segev R, Puchalla J, Berry Mn (2006) Functional organization of ganglion cells in the salamander retina. J Neurophysiol 95:2277–2292.

14. Yang G, Masland R (1994) Receptive fields and dendritic structure of directionally selective retinal ganglion cells. J Neurosci 14:5267–5280.

15. Brown S, He S, Masland R (2000) Receptive field microstructure and dendritic geometry of retinal ganglion cells. Neuron 27:371–383.

16. Passaglia C, Troy J, Ruttiger L, Lee B (2002) Orientation sensitivity of ganglion cells in primate retina. Vision Res 42:683–694.

17. Kolb H, Marshak D (2003) The midget pathways of the primate retina. Doc Ophthalmol 106:67–81.

18. Dacey D (2004) Origins of perception: retinal ganglion cell diversity and the creation of parallel visual pathways. In: Gazzaniga M, editor, The Cognitive Neurosciences, MIT Press. pp. 281–301.

19. Yamada E, Bordt A, Marshak D (2005) Wide-field ganglion cells in macaque retinas. Vis Neurosci 22:383–393.

20. Puchalla J, Schneidman E, Harris R, Berry M (2005) Redundancy in the population code of the retina. Neuron 46:493–504.

21. Polyak S (1941) The retina. Chicago: University of Chicago Press.

22. Watanabe M, Rodieck R (1989) Parasol and midget ganglion cells of the primate retina. J Comp Neurol 289:434–454.

23. Leventhal A, Rodieck R, Dreher B (1981) Retinal ganglion cell classes in the old world monkey: morphology and central projections. Science 213:1139–1142.

24. Perry V, Cowey A (1981) The morphological correlates of x- and y-like retinal ganglion cells in the retina of monkeys. Exp Brain Res 43:226–228.

25. Perry V, Oehler R, Cowey A (1984) Retinal ganglion cells that project to the dorsal lateral geniculate nucleus in the macaque monkey. Neuroscience 12:1101–1123.

26. Dacey D, Brace S (1992) A coupled network for parasol but not midget ganglion cells in the primate retina. Vis Neurosci 9:279–290.

27. Dacey D, Petersen M (1992) Dendritic field size and morphology of midget and parasol ganglion cells of the human retina. Proc Natl Acad Sci U S A 89:9666–9670.

28. Dacey D (1993) The mosaic of midget ganglion cells in the human retina. J Neurosci 13:5334–5355.

29. Livingstone M, Hubel D (1988) Segregation of form, color, movement, and depth: anatomy, physiology, and perception. Science 240:740–749.

30. Croner L, Kaplan E (1995) Receptive fields of p and m ganglion cells across the primate retina. Vision Res 35:7–24.

31. Lee B (1996) Receptive field structure in the primate retina. Vision Res 36:631–644.

32. Litke A, Bezayiff N, Chichilnisky E, Cunningham W, Dabrowski W, et al. (2004) What does the eye tell the brain? development of a system for the large scale recording of retinal output activity. IEEE Trans Nucl Sci :1434–1440.

33. Frechette E, Sher A, Grivich M, Petrusca D, Litke A, et al. (2005) Fidelity of the ensemble code for visual motion in primate retina. J Neurophysiol 94:119–135.

34. Chichilnisky E, Kalmar R (2002) Functional asymmetries in on and off ganglion cells of primate retina. J Neurosci 22:2737–2747.

35. Field G, Sher A, Gauthier J, Greschner M, Shlens J, et al. (2007) Spatial properties and functional organization of small bistratified ganglion cells in primate retina. J Neurosci 27:13261–13272.

36. Rodieck R (1965) Quantitative analysis of cat retinal ganglion cell response to visual stimuli. Vision Res 5:583–601.

37. Field G, Chichilnisky E (2007) Information processing in the primate retina: circuitry and coding. Annu Rev Neurosci 30:1–30.

38. Peichl L, Wassle H (1981) Morphological identification of on- and off-centre brisk transient (y) cells in the cat retina. Proc R Soc Lond B Biol Sci 212:139–153.

39. Peichl L, Wassle H (1983) The structural correlate of the receptive field centre of alpha ganglion cells in the cat retina. J Physiol 341:309–324.

40. Freed M, Smith R, Sterling P (1992) Computational model of the on-alpha ganglion cell receptive field based on bipolar cell circuitry. Proc Natl Acad Sci U S A 89:236–240.

41. Kier C, Buchsbaum G, Sterling P (1995) How retinal microcircuits scale for ganglion cells of different size. J Neurosci 15:7673–7683.

42. Dacey D, Packer O, Diller L, Brainard D, Peterson B, et al. (2000) Center surround receptive field structure of cone bipolar cells in primate retina. Vision Res 40:1801–1811.

43. Kolb H, Dekorver L (1991) Midget ganglion cells of the parafovea of the human retina: a study by electron microscopy and serial section reconstructions. J Comp Neurol 303:617–636.

44. Jacoby R, Wiechmann A, Amara S, Leighton B, Marshak D (2000) Diffuse bipolar cells provide input to off parasol ganglion cells in the macaque retina. J Comp Neurol 416:6–18.

45. Vincent B, Baddeley R (2003) Synaptic energy efficiency in retinal processing. Vision Res 43:1283–1290.

46. Vincent B, Baddeley R, Troscianko T, Gilchrist I (2005) Is the early visual system optimised to be energy efficient? Network 16:175–190.

47. Merigan W, Maunsell J (1993) How parallel are the primate visual pathways? Annu Rev Neurosci 16:369–402.

48. Callaway E (2005) Structure and function of parallel pathways in the primate early visual system. J Physiol 566:13–19.

49. Kaplan E, Shapley R (1986) The primate retina contains two types of ganglion cells, with high and low contrast sensitivity. Proc Natl Acad Sci U S A 83:2755–2757.

50. Lee B, Martin P, Valberg A (1989) Sensitivity of macaque retinal ganglion cells to chromatic and luminance flicker. J Physiol 414:223–243.

51. Lee B, Martin P, Valberg A (1989) Amplitude and phase of responses of macaque retinal ganglion cells to flickering stimuli. J Physiol 414:245–263.

52. Benardete E, Kaplan E, Knight B (1992) Contrast gain control in the primate retina: P cells are not x-like, some m cells are. Vis Neurosci 8:483–486.

53. De Monasterio F, Gouras P (1975) Functional properties of ganglion cells of the rhesus monkey retina. J Physiol 251:167–195.

54. Troy J, Lee B (1994) Steady discharges of macaque retinal ganglion cells. Visual Neuroscience 11:111–118.

55. Feller M, Scanziani M (2005) A precritical period for plasticity in visual cortex. Curr Opin Neurobiol 15:94–100.

56. White L, Fitzpatrick D (2007) Vision and cortical map development. Neuron 56:327–338.

57. Hooks B, Chen C (2007) Critical periods in the visual system: changing views for a model of experience-dependent plasticity. Neuron 56:312–326.

58. Chichilnisky E (2001) A simple white noise analysis of neuronal light responses. Network: Computation in Neural Systems 12:199–213.

59. Rieke F, Warland D, de Ruyter van Steveninck R, Bialek W (1997) Spikes: exploring the neural code. Cambridge, MA: MIT Press, 395 pp.

60. Thibos L, Levick W (1983) Bimodal receptive fields of cat retinal ganglion cells. Vision Res 23:1561–1572.

61. Wassle H, Peichl L, Boycott B (1981) Dendritic territories of cat retinal ganglion cells. Nature 292:344–345.

62. Dacey D (1989) Monoamine-accumulating ganglion cell type of the cat's retina. J Comp Neurol 288:59–80.

63. Levick W, Thibos L (1982) Analysis of orientation bias in cat retina. J Physiol 329:243–261.

64. Braccini C, Gambardella G, Sandini G, Tagliasco V (1982) A model of the early stages of the human visual system: functional and topological transformations performed in the peripheral visual field. Biol Cybern 44:47–58.

65. Watson A, Ahumada AJ (1989) A hexagonal orthogonal-oriented pyramid as a model of image representation in visual cortex. IEEE Trans Biomed Eng 36:97–106.

66. Blakemore C, Adler K, Pointon M (1993) Vision: Coding and Efficiency. Cambridge University Press.

67. Masland R (2001) The fundamental plan of the retina. Nat Neurosci 4:877–886.

68. Milam A, Dacey D, Dizhoor A (1993) Recoverin immunoreactivity in mammalian cone bipolar cells. Vis Neurosci 10:1–12.

69. Cohen E, Sterling P (1991) Microcircuitry related to the receptive field center of the on-beta ganglion cell. J Neurophysiol 65:352–359.

70. Lin B, Martin P, Grunert U (2002) Expression and distribution of ionotropic glutamate receptor subunits on parasol ganglion cells in the primate retina. Vis Neurosci 19:453–465.

71. Lukasiewicz P (2005) Synaptic mechanisms that shape visual signaling at the inner retina. Prog Brain Res 147:205–218.

72. Sernagor E, Eglen S, Wong R (2001) Development of retinal ganglion cell structure and function. Prog Retin Eye Res 20:139–174.

73. Shadlen M, Newsome W (1998) The variable discharge of cortical neurons: implications for connectivity, computation, and information coding. J Neurosci 18:3870–3896.

74. Baker S, Spinks R, Jackson A, Lemon R (2001) Synchronization in monkey motor cortex during a precision grip task. i. task-dependent modulation in single-unit synchrony. J Neurophysiol 85:869–885.

75. Cohen D, Nicolelis M (2004) Reduction of single-neuron firing uncertainty by cortical ensembles during motor skill learning. J Neurosci 24:3574–3582.

76. Harris K (2005) Neural signatures of cell assembly organization. Nat Rev Neurosci 6:399–407.

77. Zhan X, Troy J (2000) Modeling cat retinal beta-cell arrays. Vis Neurosci 17:23–39.

78. Goodchild A, Ghosh K, Martin P (1996) Comparison of photoreceptor spatial density and ganglion cell morphology in the retina of human, macaque monkey, cat, and the marmoset callithrix jacchus. J Comp Neurol 366:55–75.

79. Chichilnisky E, Baylor D (1999) Receptive-field microstructure of blue-yellow ganglion cells in primate retina. Nature Neurosci 2:889–893.

80. Haverkamp S, Grunert U, Wassle H (2001) The synaptic architecture of ampa receptors at the cone pedicle of the primate retina. J Neurosci 21:2488–2500.

81. Klug K, Herr S, Ngo I, Sterling P, Schein S (2003) Macaque retina contains an s-cone off midget pathway. J Neurosci 23:9881–9887.

82. Borghuis B, Ratliff C, Smith R, Sterling P, Balasubramanian V (2008) Design of a neuronal array. J Neurosci 28:3178–3189.